TÉCNICO LISBOA

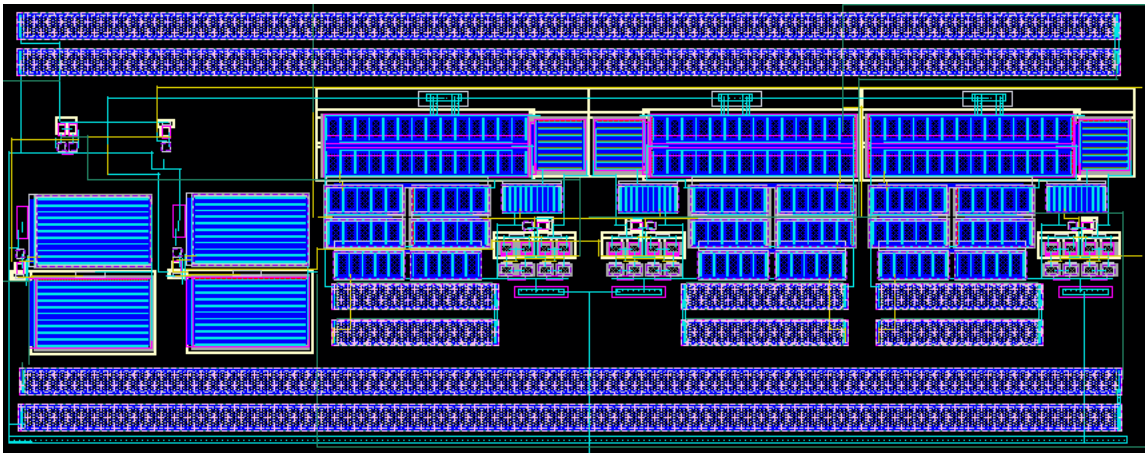

Light-Harvesting Battery Charger for IoT Sensor Node

Maísa Santos Craveiro Seidi

Thesis to obtain the Master of Science Degree in

Electrical and Computer Engineering

Supervisors: Prof. João Manuel Torres Caldinhas Simões Vaz
Prof. Pedro Nuno Mendonça dos Santos

Examination Committee

Chairperson: Prof. Teresa Maria Canavarro Menéres Mendes de Almeida
Supervisor: Prof. Pedro Nuno Mendonça dos Santos
Member of the Committee: Prof. Marcelino Bicho dos Santos

June 2023

Declaração

Declaro que o presente documento é um trabalho original da minha autoria e que cumpre todos os requisitos do Código de Conduta e Boas Práticas da Universidade de Lisboa.

Declaration

I declare that this document is an original work of my own authorship and that it fulfils all the requirements of the Code of Conduct and Good Practices of the Universidade de Lisboa.

Acknowledgments

First and foremost, I would like to express my deepest appreciation and thanks to my supervisors professor Pedro Santos and professor João Vaz, for their invaluable guidance and relentless support throughout the course of this work. A special thanks to *Instituto de Telecomunicações* and the *Wireless Circuits - Lx* group for granting me this research opportunity and for providing me with all the necessary equipment to conduct this study.

I would also like to extend my deepest gratitude to Instituto Camões, I.P., for awarding me with a scholarship that proved itself to be a substantial support during these last few years.

I cannot leave Instituto Superior Técnico without mentioning Rita Wahl and NDA, who's support and assistance were of great value, especially in the most difficult times.

Special thanks to all the colleagues and friends who were by my side throughout this journey, making it somehow easier, and to the professors that played a role in my academic career.

The completion of this degree would not have been possible without the relentless support and nurturing of my family: my mother, my brother, my sister, my aunt, friends and relatives, thank you for your trust and unwavering belief in me. To my father, thank you for inspiring me and giving me the strength to complete this chapter.

Last but not least, thank you to my Jazzy friends for your endless support and amazing energy that brightened the end of this journey in the most beautiful way.

Resumo

O rápido desenvolvimento da Internet das Coisas traz uma elevada procura por microssistemas mais eficientes e autónomos, sistemas esses presentes em vários dispositivos como sensores, *wearables* e aplicações biomédicas. Esses dispositivos são geralmente alimentados por pequenas baterias, e a duração limitada das mesmas impõe uma restrição na duração da operação desses sistemas. A colheita de energia constitui um meio prático para aumentar a autonomia destes microssistemas, através da utilização da energia capturada de fontes de energia renováveis e da sua conversão em energia elétrica útil para alimentar esses circuitos.

O objetivo desta dissertação é projetar um carregador de bateria *light-harvesting* que usa a energia capturada por um painel fotovoltaico para carregar uma bateria NiMH de 1.2 V, que é por sua vez usada para alimentar um nó de um sensor *IoT*. O design completo é realizado numa tecnologia CMOS de 65 nm. Um modelo equivalente da bateria, pronto para simulação, é desenvolvido com base em procedimentos experimentais. O projeto e a implementação do sistema completo é apresentado e testado em simulação. Técnicas de gestão da bateria com proteção contra sobrecarga e sobredescarga são incorporadas. Finalmente, um *layout* completo do sistema é proposto e testado em simulação, juntamente com os modelos de fonte e bateria desenvolvidos, para diferentes condições de operação.

Palavras Chave

Carregador de bateria; Colheita de energia; Modelo elétrico de bateria; Internet das Coisas; Tecnologia CMOS; Células solares.

Abstract

The rapid development of the Internet of Things brings a high demand for more efficient and autonomous micro-systems, used in several devices such as sensors, wearables and biomedical applications. These devices are generally powered by small batteries, and the limited battery life imposes a constraint in the duration of their operation. Energy harvesting presents a practical means to increase the autonomy of these micro-systems, by using the captured energy from renewable energy sources and converting them into usable electrical energy to power these circuits.

This dissertation's objective is to design a light-harvesting battery charger that uses the energy captured by a photovoltaic cell to charge a 1.2 V nominal voltage NiMH battery, that is used to supply an IoT sensor node. The whole system is developed in a CMOS 65nm proccess. A simulation-ready equivalent model for the battery is developed based on experimental procedures. The design and implementation of the full system is presented and tested in simulation. Battery management with overcharge and over-discharge protection for the battery are incorporated. Finally, a pos-layout simulation is performed, along with the source and battery models developed, for various operation conditions.

Keywords

Battery charger; Light-harvesting; Battery electrical model; Internet of Things; CMOS technology; Solar cells.

Contents

List of Tables

List of Figures

Acronyms

AC	Alternating current
Ah	Ampere-hour
BGR	Bangdap voltage reference
CC-CV	Constant-current constant-voltage
CMOS	Complementary metal–oxide–semiconductor
DC-DC	Direct current - direct current
DC	Direct current
EOC	End of charge
EOD	End of discharge
IC	Integrated circuit
IoT	Internet of Things
Isc	Short-circuit current
LDO	Low dropout regulator
Li-ion	Lithium-ion
mAh	Milliampere hour
MOS	Metal–oxide–semiconductor
MPPT	Maximum power point tracking
MPP	Maximum power point
NiMH	Nickel–metal hydride
NMOS	N-channel metal-oxide semiconductor
OpAmp	Operational Amplifier
PMIC	Power management integrated circuit
PMOS	P-channel metal-oxide semiconductor

PV	Photovoltaic
PWM	Pulse width modulation
SC	Switched capacitors
SOC	State of charge
SOIC	Small outline integrated circuit
VCO	Voltage controlled oscillator
Voc	Open-circuit voltage

1

Introduction

Contents

1.1 Motivation

The Internet of Things (IoT) can be defined as a comprehensive network in which objects such as sensors, actuators, and processors communicate with each other to serve a meaningful purpose. These electronic devices are typically powered by small batteries and although some low power applications only require between 10 µW to 10 mW to operate [1], the limited battery lifetime imposes a limitation on the durability of these devices.

Despite the technological advances accomplished in recent years, the improvements related to energy density for batteries is still slow, requiring larger batteries for longer lifetime, which can be unfeasible in small portable devices [2]. Additionally, the attempts to counterbalance the battery lifetime limitation by reducing the devices' power demand are constrained by the limitations of the semiconductor technology scaling in terms of reducing the power consumption of analog and digital circuits [2]. Considering the complexity and large number of distributed devices across the IoT network, often times in inaccessible locations, recharging or replacing thousands of batteries can be an impracticable solution [3].

Energy harvesting presents itself as an efficient way to power and recharge these devices, by alleviating the cost and difficulty of wiring a large number of these objects [4]. The ability to use the energy harvested from the environment to produce usable electric energy that can power these devices provides a practical solution for more autonomous self-powered IoT nodes, that can become less dependent on external power sources.

Several energy sources can be used for this purpose such as light, motion, heat, vibration and others. Out of the above, light harvesting is typically the most popular option due to its abundance and higher power density in comparison with the alternative sources [5]. Notwithstanding, there are some limitations to light-harvested energy. First and foremost, the energy source is intermittent, given that sunlight is not always available, indoor light can be a poor substitute and additionally, small Photovoltaic (PV) cells capture only a small fraction of the available light. Consequently, these light-harvesting systems are not sufficient to feed the devices on their own; a storage device, such as a battery, should be used to store the energy for a continuous and reliable operation of these electronic circuits [1].

In this sense, it is of special interest the research on light-harvesting systems, capable of operating over a wide input power range, to account for changes in the environmental conditions [6] and to efficiently power rechargeable batteries for IoT sensor nodes.

1.2 Objectives

The purpose of this research is to design a fully integrated light-harvesting system, capable of charging a small Nickel–metal hydride (NiMH) battery, that is used to power an IoT sensor node. The full system is designed using a 65 nm Complementary metal–oxide–semiconductor (CMOS) process.

The harvester receives energy from a PV cell, and constantly monitors the energy available in the environment and the battery's State of charge (SOC), to decide when the system should be switched on to charge the battery, and when the battery is in the right conditions to feed the final load. Figure 1.1 presents a top illustration of the system and its connections to the PV cell, the battery and the final load. This study focuses on the design of the fully integrated system that is enclosed in the blue box represented on the figure.

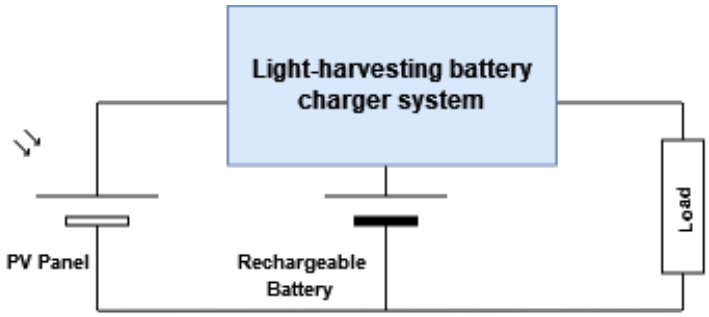

Figure 1.1: Illustration of the top system to be designed.

The system's main specifications are presented below:

- Input energy source: ONP1.2-12x24 Solar Panel;
- Battery: V6HR Varta microbattery;
- Output load: 100 Ω - 100 kΩ resistive load;
- The full system should be supplied by the battery.

Below is a summary of some relevant characteristics of the devices.

ONP1.2-12x24 Solar Panel

- Average Open-circuit voltage (Voc): 1.6 V
- Maximum Voc: 1.9 V
- Short-circuit current (Isc): 4.3 mA
- Nominal operating conditions under full sun: 3.3 mA at 1.2 V

V6HR Microbattery

- Nominal voltage: 1.2 V
- Capacity: 6.2 mAh
- Approximate End of charge (EOC) voltage: 1.5 V
- Approximate End of discharge (EOD) voltage: 0.9 V

1.3 Structure

This thesis is divided into six essential chapters. In this first chapter, an introduction to the conducted research was presented, along with the motivation and objectives for this study.

The second chapter gives an overview of the latest and most relevant work carried out in this area, and explains what specific topics the present work intends to study.

The third chapter presents the models developed for the battery and the PV panel, and explains the experimental and computational procedures performed to obtain these models.

On the fourth chapter, the system design is presented, each block is described and analyzed individually, and the final layout of the integrated system is shown.

The fifth chapter presents the results obtained for the final simulation of the harvester, along with the models developed for the PV panel and the battery. The system's operation is verified for different temperatures and conditions, using the corners analysis.

Lastly, the final conclusions of this study are presented, and grounds for future work in this area are suggested.

2

Energy-harvesting Battery Charging Systems

Contents

2.1 State of the Art

Light-harvesting CMOS battery chargers use the Direct current (DC) voltage produced by PV cells to charge the batteries. In most systems, buck/boost converters are used with the purpose of adjusting the voltage levels required by the battery. Battery management with overcharge and overdischarge protection mechanisms are usually required to ensure a safe operation. Some systems also use Maximum power point tracking (MPPT) to maximize the efficiency. A brief description of some available systems is presented hereafter.

The work developed in [7] presents an efficient battery charging system that can either use an energy-harvesting source, or an Alternating current (AC) adapter, as power supply. The system uses a pulse-charge as an alternative to the conventional Constant-current constant-voltage (CC-CV) charging method. The pulse-charge incorporates over-voltage protection, and can operate in trickle charge, fast charge or slow charge mode, depending on the battery's state. Additionally, a power path controller is used to select the optimal charging source, and a step down Direct current - direct current (DC-DC) converter is implemented to reduce the battery's voltage and provide power for the energy-harvesting system's startup. The pulse-charge frequency is optimized based on the experimentally obtained characteristics of the battery. This system, which is implemented on a CMOS 0.18 μm technology process, ensures a battery charge efficiency improvement of 3.15% and a charge time reduction of 37.35% for a 100 mAh Lithium-ion (Li-ion) battery.

Paper [5] presents a 0.35 μm CMOS process power management system for light-harvesting applications, that addresses the different possible lightning conditions, using an adaptive step-up voltage scheme. The power management circuit comprises an inductor-less charge pump that is used to step-up the voltage when the PV cell is under low lightning conditions, and the generated voltage is insufficient to charge the battery. An optimal power tracking unit is implemented to estimate the operating parameters that maximize the system's output power. The operating parameters are tuned through a control unit which uses a Voltage controlled oscillator (VCO) to generate a variable clock frequency for the charge pump.

The battery charger in [8] proposes a mixed-signal system that integrates MPPT with battery management to increase the efficiency and ensure safe charging/discharging for the battery. An off-chip Low dropout regulator (LDO) is used to provide the necessary voltage levels for the circuits' operation, and a ring oscillator generates the system's clock signal. Start-up circuits are also present and a Pulse width modulation (PWM) controller is used to generate the duty cycles for the Metal–oxide–semiconductor (MOS) switches. A stable charging voltage of 4.2 V is produced on the maximum power point, from input voltages in the range of 0.5 V to 2 V. The charging and discharging currents are measured, and comparators are used to monitor the battery's voltage to prevent overcharge and overdischarge, using externally generated voltage references.

A solar energy harvester based on a Power management integrated circuit (PMIC) is proposed in [4]. The harvester and battery charger integrates MPPT, as well as battery overvoltage and undervoltage protection, with user-configurable threshold voltages and integrated buck-boost and boost capabilities, that are able to regulate the voltage supplied to the load. The system uses the SPV1050 PMIC, has a peak solar cell power output of 24.5 mW, a storage capacity of 33 mWh, and an output voltage of 1.8 V.

The work in [9] describes a charger that can extract energy from solar panels as well as from thermoelectric generators. The charger is a synchronous rectifier boost converter, that employs a hysteretic mode of control for regulation. It uses a sampled architecture with clock gating, power gating and sub-regulated rails, which provides low current, thus increasing the overall efficiency of the circuit. The system integrates boost converters to change voltage levels, and to cold start the circuit when the battery is deeply discharged. Battery management is also implemented, with voltage and temperature monitoring to ensure a safe operation. A state-machine is used as a control unit to provide the timing and control signals, along with an oscillator, bias generator, power on reset and charge pumps.

Paper [3] proposes a 0.18-µm CMOS system that draws energy from a PV cell to supply a 1m W load, while simultaneously using the excess power to recharge a battery. When the PV cell's power is not enough to supply the load, the battery is used instead. To account for the voltage differences across the PV cell, the battery and the load, this system uses inductor based boost and buck circuits. The initial 0.27-0.32 V supplied by the PV cell is boosted to 1.4–1.8 V to charge the battery, and a buck circuit is used to reduce the 1.4 – 1.8 V to 1 V sustained by the load. The die occupies an area of 610 $\times$ 610 – μm^2, which is integrated in a Small outline integrated circuit (SOIC) package that contains the super capacitor used as battery, the PV cell, some additional components to the system, as well as inductors and capacitors that are external to the Integrated circuit (IC).

In [10], a fully integrated solar energy harvester battery charger, implemented in a 0.18 μm CMOS process, is presented. A direct charging method is used, without the presence of DC-DC converters. The charger ensures overcharge and overdicharge protection through a voltage level detector that uses a Bangdap voltage reference (BGR) circuit to generate the reference voltages. A dynamic comparator is used to periodically monitor the difference between the PV cell and the battery's terminal voltages, and decide when the switch should be turned on to charge the battery. A bias circuit, a current-starved ring oscillator and a digital control unit are implemented to provide the required bias and control signals for the circuits, and a linear regulator is used to reduce the supply voltage for the digital blocks. The system was tested with a battery with EOC and EOD voltages that range from 3 V to 4.3 V, presenting a power consumption of around 300 nW, in a die area of 0.12 mm^2.

Article [6] proposes an energy-harvesting battery charger IC, fabricated in a 0.25 μm CMOS process, capable of charging a 3 V battery, from an input source ranging from 0.3 – 2 V. It uses a frequency-sweeping input power monitor, allowing it to operate with high efficiency over a wide input power range,

by simultaneously ensuring low power consumption and fast response time. A clocked comparator is periodically triggered by a variable frequency clock signal to compare the input voltage with the reference voltage and decide when the charge transfer should start. The system uses a boost converter, pulse generator blocks, current and voltage reference circuits and an oscillator with an exponentially decaying frequency for the input power monitor.

A 0.18 μm CMOS process energy-harvesting circuit is presented in [11], capable of charging a battery from 1.8 to 3.3 V, from an input voltage range of 100 mV to 2.5 V, with MPPT. In order to maximize the converter efficiency across a wide range of input voltage, a technique is employed to analytically obtain the optimal inductor energizing time. A digital asynchronous burst mode controller is used to reduce the power consumption of the input comparator, and a capacitor-less *sample and hold* circuit is implemented to reduce the leakage otherwise present in conventional MPPT systems. The system also employs battery management techniques for over and undervoltage protection, with timing signals generated by a low-power relaxation oscillator. The voltage references are internally generated and off-chip resistors are used to offer programmable values.

A 0.25 μm standard CMOS process energy-harvesting power supply for mobile applications is proposed in [2]. The system employs MPPT and generates a regulated power supply through a single power conversion stage. A CC-CV charging mode is implemented to ensure safe charging and a monitoring mechanism is employed to control the load supply and battery charging, depending on the available harvested energy.

The paper on [12] proposes a fast waking charger that is more efficient during wake-up than most available systems. The circuit consists of a switched-inductor harvester, implemented in 0.18 μm CMOS technology. The system draws power from a thermogenerator or light-harvesting source to charge a small temporary capacitor up to a certain level, and then use this capacitor to feed an off-chip battery or circuit. Considering that small capacitors charge faster and that transistors switch faster while dissipating less power when supplied with higher voltages, this technique improves the efficiency of the charging system. The system uses a boost DC-DC converter to adjust the voltage level, and an oscillator pulse generator to control the charging cycles. A starter circuit is implemented to charge the small capacitor when the system is initially supplied after a long drought. A bias circuit is used to provide the required voltage levels for the blocks, and a controller circuit is also present to decide when to disable the starter circuit and enable the oscillator pulse generator, when to charge the temporary capacitor, and when to use the battery to supply the system.

Table 2.1 presents a short summary of the main characteristics of the previously discussed works.

Table 2.1: Comparison table between the state of the art works

Design	CMOS Technology	Input voltage	Battery voltage	Layou Area
[7]	0.18 um	3.3 V	3 V	4 mm^2
[5]	0.35 um	NA	NA	0.043 mm^2
[8]	0.35 um	0.5 - 2 V	4.2 V	1.44 mm^2
[4]	Discrete circuit	150 mV - 4.46 V	2.6 - 5.3 V	6 mm^2 (SPV1050 only)
[9]	NA	330 mV	3 V	NA
[3]	0.18 um	0.27-0.32 V	1.8 V	0.37 um^2
[1]	0.18 um	3-5.5 V	3-4.3 V	0.12 mm^2
[11]	0.18 um	100 mV - 2.5 V	1.8 - 3.3 V	2.54 mm^2
[2]	0.25 um	7 V	1.8 V	NA
[12]	0.18 um	350 mV	0.9 V	na
[6]	0.25 um	0.3 - 3 V	2.5 - 4.1 V	0.07 mm^2

2.2 Proposed system

Figure 2.1 presents the architecture of the system to be implemented.

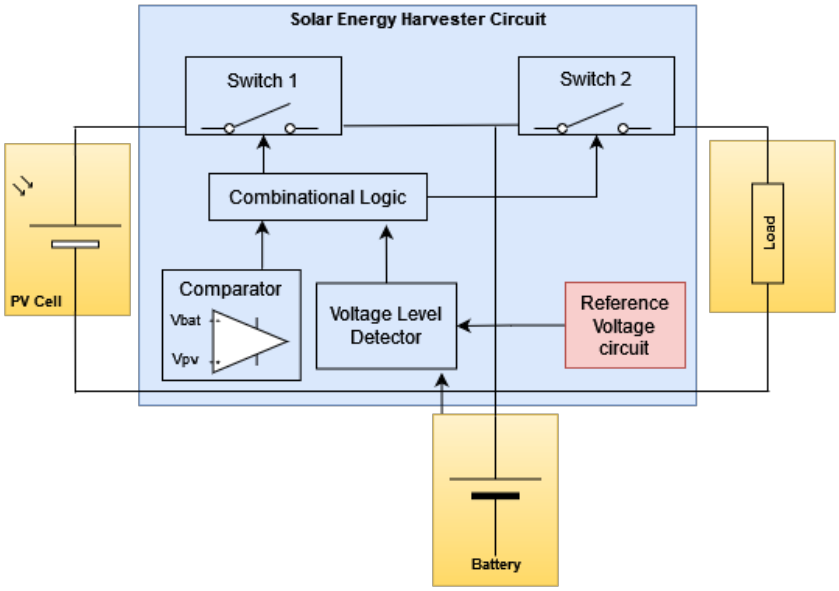

Figure 2.1: Block diagram of the proposed system.

The system proposed on this thesis focuses on the development of a fully integrated simple light-harvesting battery charger, with battery management techniques that ensure overcharge and overdischarge protection. Figure 2.2 presents a classification of all of the latest works previously addressed in the *State of the Art* and frames the present work according to the main characteristics that distinguishes it from the remaining systems developed so far.

The leading reference for this work is the harvester presented in [1], however some different approaches were adopted in the development of this system, which prioritizes a lower complexity and the

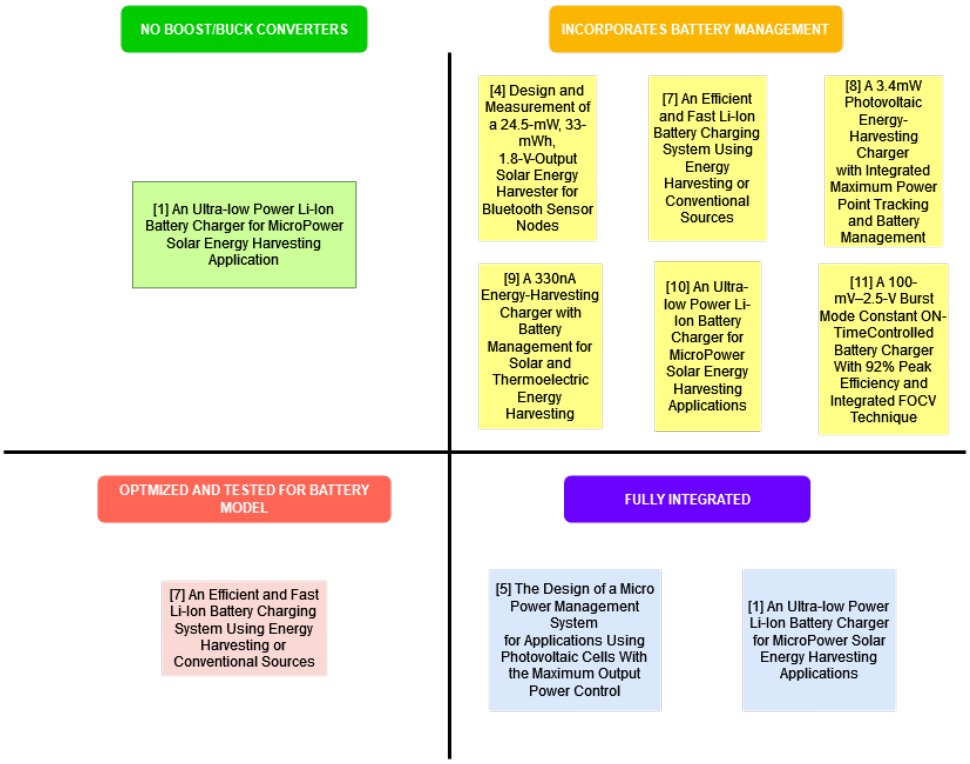

Figure 2.2: Classification of the different works discussed in the *State of the Art*.

study of the source and battery equivalent electrical models. The charger proposed here is optimized for an experimentally obtained electrical model of a NiMH battery, and both the model of the energy source and of the battery are used for testing in simulation, which ensures a more accurate estimate of the system's real behavior on silicon. No buck/boost converters are used in this implementation. These circuits either require a big area, or a high operation frequency to function properly, thus increasing the power consumption and the substrate noise of the system. For this reason, the system developed here presents a much lower area when compared to the alternative approaches, and no high-frequency generated noise components in the substrate. Moreover, it is the only system developed in a CMOS 65 nm process. Finally, the required reference voltages design, which are usually generated using a BGR circuit, were considered out of the scope of this study.

3

Battery and Source Modeling

Contents

3.1 Battery Characterization and Modeling

The characterization of the battery is essential for the development of a simulation-ready equivalent electrical circuit model that can be considered in the design of the solar harvester, allowing it to be optimized for the electrical characteristics of the battery under study. In order to obtain the theoretical model, it is necessary to carry out experimental tests that allows for the estimation of the parameters of the equivalent circuit. This section presents the chosen model and the experimental procedure adopted to obtain the battery's equivalent circuit.

3.1.1 Electrical model of the battery

Before diving into the battery's equivalent model, it is important to present some relevant definitions which are considered in the study of the battery.

Capacity

The battery's capacity is defined as the amount of electrical energy that the battery can supply to the load, at a constant current rate, during a specific time length. It is measured in Milliampere hour (mAh), although mAh is energy/Volt.

End of Discharge Voltage (V_{EOD})

The EOD voltage corresponds to the battery's terminal voltage after being fully discharged. It depends on the discharge rate and temperature.

End of Charge Voltage (V_{EOC})

The EOC voltage corresponds to the battery's terminal voltage after being fully charged. It depends on the charge rate and temperature.

Several electrical equivalent models for batteries have been proposed by different authors. A detailed analysis and comparison of these various models is presented in [13]. For the purpose of this work, the electrical circuit model proposed in [14] is considered, as it is the most complete model and the one which best represents the dynamic characteristics of the battery. This model prevails by providing a very good approximation of the electrical characteristics that represents the battery's operation, accurately reflecting the battery's run time, as well as its stationary and transient responses. Theoretically, all the parameters in the model are multi-variable functions of the SOC, current, temperature, and cycle number (the number of charge and discharge cycles). Figure 3.1 presents the electrical model in question.

The presented model can be subdivided into two distinct branches: one that simulates the battery's run-time and another that represents its transient response and the V-I characteristic.

The first branch on the left is constituted by a self-discharge resistor that reflects the energy losses that occur when the battery is not being used for a long period of time, due to chemical processes

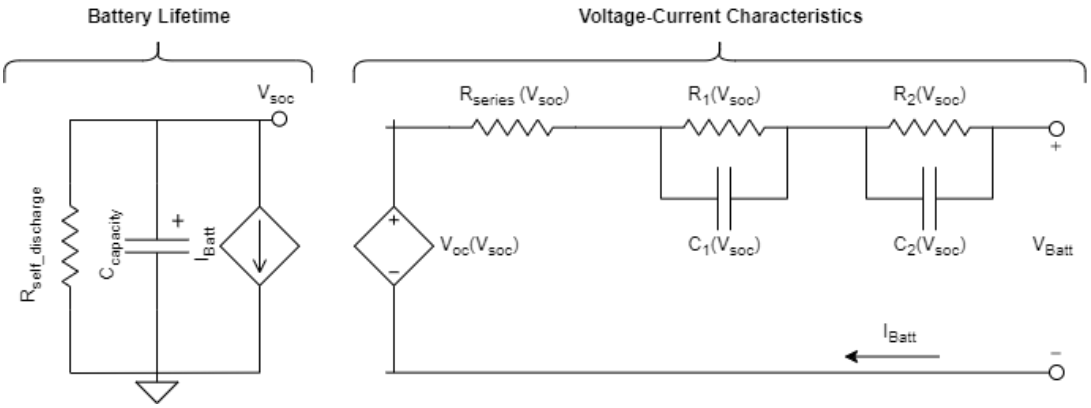

Figure 3.1: Electrical model used for the battery.

inherent to its constitution. In parallel with this resistor there is a capacitor that represents the full capacity or energy stored in the battery, at a given moment. This capacitor's value is defined as in equation 3.1.

$$C_{capacity} = 3600 \times C_{nom} \times f_1(\text{Cycle}) \times f_2(\text{Temp}) \text{ [C]} \tag{3.1}$$

where C_{nom} is the nominal capacity in Ampere-hour (Ah) and f1 (Cycle) and f2 (Temp) represent the battery's charge variation with the number of cycles and with the temperature, respectively. For the purpose of this work, the parameters' dependence with the number of cycles and temperature are ignored, since they have negligible effects, and because including them would significantly increase the complexity of the test system.

The voltage V_{SOC} quantitatively represents the state of charge of the battery, taking values between 0 (battery fully discharged) and 1 (battery fully charged). The dependent current source serves to charge or discharge the capacitor, dynamically changing the voltage V_{SOC}, thus modeling the relationship between the state of charge of the battery and the current.

The branch on the right represents the V-I characteristic of the battery. The dependent voltage source describes the non-linear relationship between the open circuit voltage and the battery's state of charge. The series resistance represents the internal resistance of the battery and the RC branches simulate the relaxation effects, with the first branch representing the short time constant and the second branch the long time constant of the battery. It should be noted that more parallel RC branches can be used to improve the accuracy of the model, at the cost of an increase in the analysis' complexity. For the application in question, it is considered that the use of two branches is sufficient for the intended results.

3.1.2 Experimental Procedure

To estimate the values of the parameters of the battery's equivalent model, it was necessary to resort to an experimental procedure that allowed for the collection of adequate data for their computation. Figure 3.2 illustrates the test system set up for the experiment.

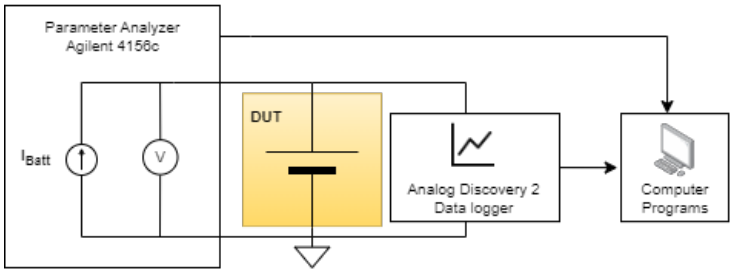

Figure 3.2: Battery test system.

Previous works [15], [16] and [17] present different methods to obtain an equivalent model for the battery. After thoroughly studying and considering all these methods, a suitable procedure was developed for this work.

The carried out test consisted on applying charging and discharging cycles to the battery and subsequently observing its terminal voltage variation. A current-controlled charge/discharge method was used, with the aid of the *Agilent 4156c Precision Semiconductor Parameter Analyzer* [18], controlled through the *EasyEXPERT* computer software. A test system was programmed in the equipment so that current pulses were applied to the battery to either charge or discharge it, in a timely manner, while measuring the terminal voltage of the battery. Since the experimental tests took a considerable amount of time, the *Analog Discovery 2* [19] board was simultaneously used as a data logger to continuously measure and store the battery's terminal voltage.

Initially, a 16-hour charge was carried out, with a current of 0.1C (0.620 mA), according to the manufacturer's instructions, to ensure that the battery was fully charged with a SOC of 100%. After charging, a rest time is required for the battery to reach equilibrium, and for the open circuit voltage to be measured, so a waiting time of one hour was established.

With the battery fully charged, a discharge with current pulses was then carried out. The purpose of using this charge/discharge method is to analyze, for different battery charge states, its transient behavior, in order to obtain the parameters of the equivalent model, since these vary with the battery's state of charge. Pulses of 1C (6.2 mA - rated current) with a duration of 10 minutes and intervals of 10 minutes between each pulse were selected, considering that to be a sufficient time for voltage stabilization. The purpose of this test is to discharge the battery from 100% to 0% and observe the evolution of the voltage in the interval between pulses. This way, it is possible to obtain the parameter values and the open circuit voltage of the battery for each value of the state of charge. After the discharge

test, the same procedure was applied to charge the battery with current pulses of 10 minutes, with the nominal value, followed by intervals of 10 minutes, until the battery was 100% charged.

It should be noted that the time required for the battery to fully reach the steady state is approximately 5 hours. However, this delay leads to extensive tests, requiring several days for a charge or discharge cycle to be completed. For this reason, a shorter interval of 10 minutes was chosen.

3.1.3 Model Extraction

As previously mentioned, the parameters of the equivalent model are not static, varying with the SOC, current, temperature and cycle number of the battery. For simplicity, only the SOC variation is accounted for in this model. The results obtained experimentally allow for the estimation of these parameters for different points of the state of charge, through the analysis of the battery's voltage after the application of each charge/discharge pulse. The method used here is based mainly on the one presented in [20].

Figure 3.3 presents a close up of one area of the pulse-discharge graph, where the evolution of the voltage at the battery's terminals resulting from the application of the pulse discharge can be observed in more detail. This figure shows the time frame used to compute the battery's parameters, following the procedure described below.

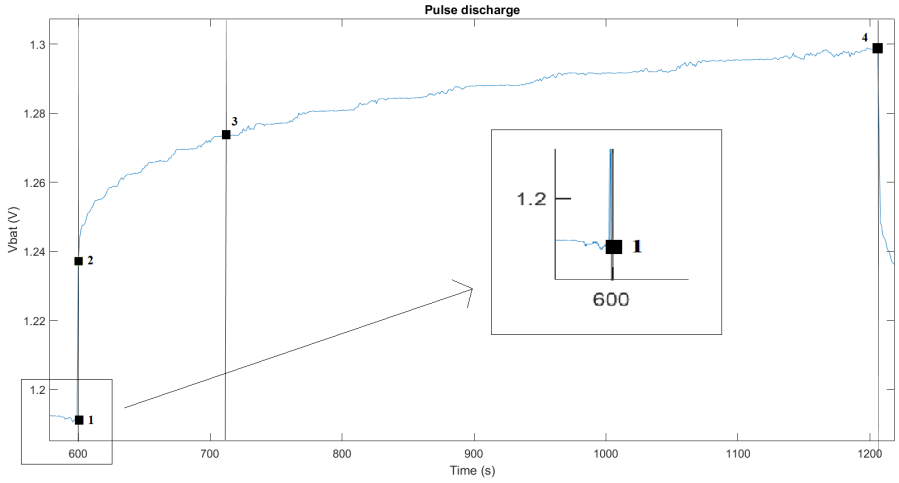

Figure 3.3: Points used in the computation of the equivalent circuit's parameters.

Analyzing the figure, a linear decrease in the voltage value is observed during the first 10 minutes, caused by the constant current discharge. When the pulse is interrupted, the sudden increase in voltage is due to the absence of current in the resistor R_{series}, which allows to obtain its value through

$$R_{series} = \frac{V_2 - V_1}{I} \tag{3.2}$$

where I is the discharge current and V_1 and V_2 are the voltages at points 1 and 2, respectively. The remaining parameters are estimated by fitting the transient response curve of the relaxation zone with an exponential function. By using an exponential function to describe the voltage between points 2 and 4, according to equation 3.3 , it's possible to extract the slow and long time constants according to the expressions in 3.4.

$$V_{bat} = v_0(t) + v_1(t)e^{-\frac{t}{\tau_1}} + v_2(t)e^{-\frac{t}{\tau_2}} \tag{3.3}$$

$$\tau_1 = R_1C_1 \quad \tau_2 = R_2C_2 \tag{3.4}$$

Using a computational calculation software, the experimentally acquired data was processed and the relaxation curves were individually adjusted with exponential functions, according to the points defined in figure 3.3. Tables 3.1 and 3.2 present the results obtained for the model parameters, for the different stages of the SOC during both discharge and charge, respectively.

Table 3.1: Extracted parameters for the discharge model of the battery.

SOC (%)	Rseries (Ω)	R1 (Ω)	C1 (F)	R2 (Ω)	C2 (F)
100.0	7.58	9.91	0.099	7.42	28.85
83.3	8.71	6.80	0.151	7.30	26.71
66.7	7.42	3.31	6.919	7.87	39.57
50.0	9.84	9.88	0.094	9.15	21.10
33.3	11.94	6.39	0.707	10.05	24.64
16.7	25.02	7.56	0.007	12.95	14.46
0.0	115.00	414.03	0.022	95.23	0.69

Table 3.2: Extracted parameters for the charge model of the battery.

SOC (%)	Rseries (Ω)	R1 (Ω)	C1 (F)	R2 (Ω)	C2 (F)
0.0	9.84	11.83	0.157	9.07	23.98
14.3	7.74	9.98	0.091	7.66	27.61
28.6	8.06	6.30	0.282	7.21	28.52
42.9	8.06	9.71	0.173	8.45	22.35
57.1	7.42	8.11	0.007	11.91	15.19
71.4	8.23	7.24	0.007	16.65	13.49
85.7	9.35	5.37	2.907	17.77	20.22
100.0	9.84	4.99	4.496	16.37	22.06

Figures 3.4 and 3.5 present V_{OC}'s variation with V_{SOC} for both charge and discharge, respectively. To illustrate this relationship, the SOC in percentage was already converted into a voltage between 0 V and 1 V. A 7th order polynomial was fitted to the above mentioned curves, as described in 3.5, to derive the open circuit voltage's dependence with the state of charge.

$$V_{OC} = p_1 V_{SOC}^7 + p_2 V_{SOC}^6 + p_3 V_{SOC}^5 + p_4 V_{SOC}^4 + p_5 V_{SOC}^3 + p_6 V_{SOC}^2 + p_7 V_{SOC} + p_8 \quad (3.5)$$

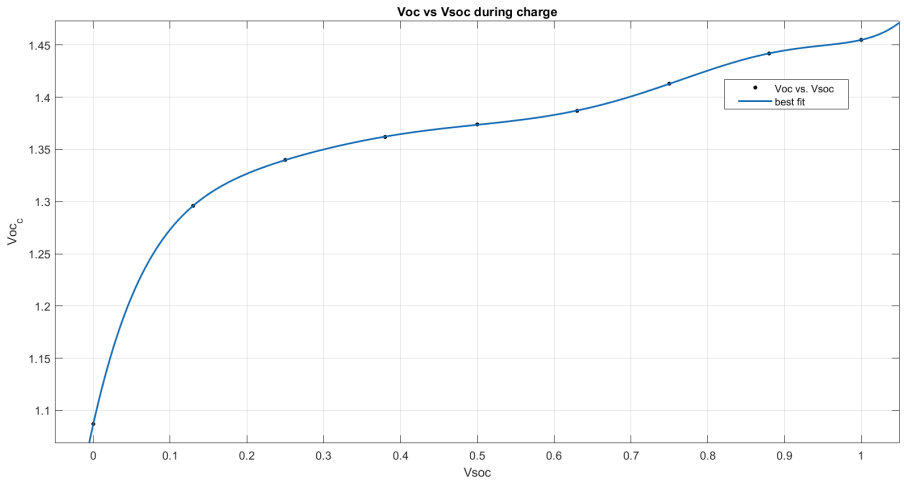

Figure 3.4: V_{OC}'s variation with V_{SOC} during charge.

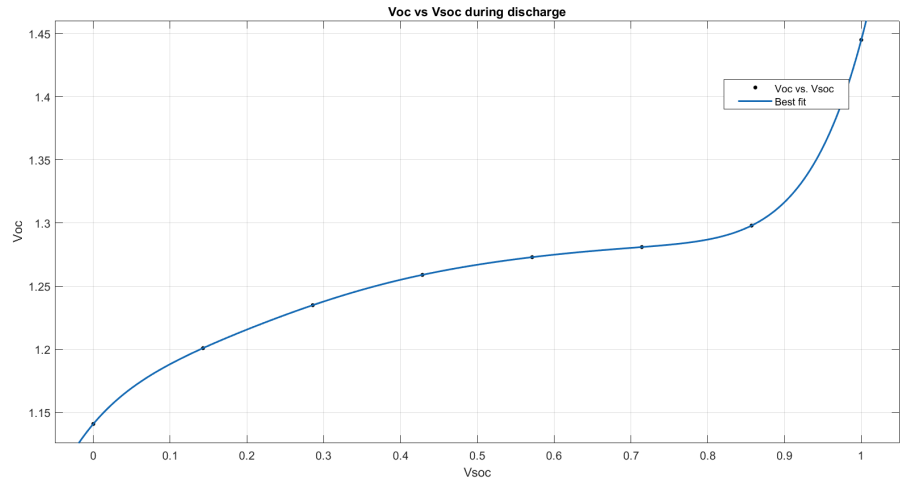

Figure 3.5: V_{OC}'s variation with V_{SOC} during discharge.

The coefficients obtained for each of the two models with 95% confidence bounds and an R-square of 1 are presented in table 3.3.

3.1.4 Model Simulation

The extracted model was implemented in Cadence Virtuoso and an analogous simulation to the experimental procedure was carried out, to assess the model's behaviour and its accuracy in comparison to

Table 3.3: Coefficients for the polynomial describing V_{OC}'s variation with V_{SOC} for charge and discharge.

Coefficients	Charge	Discharge
p_1	31.44	16.5
p_2	-121.6	-51.63
p_3	190.2	66.29
p_4	-156	-44.65
p_5	73.12	16.84
p_6	-20.16	-3.771
p_7	3.285	0.7205
p_8	1.087	1.141

the laboratory results. The general model of the battery is presented in figure 3.6.

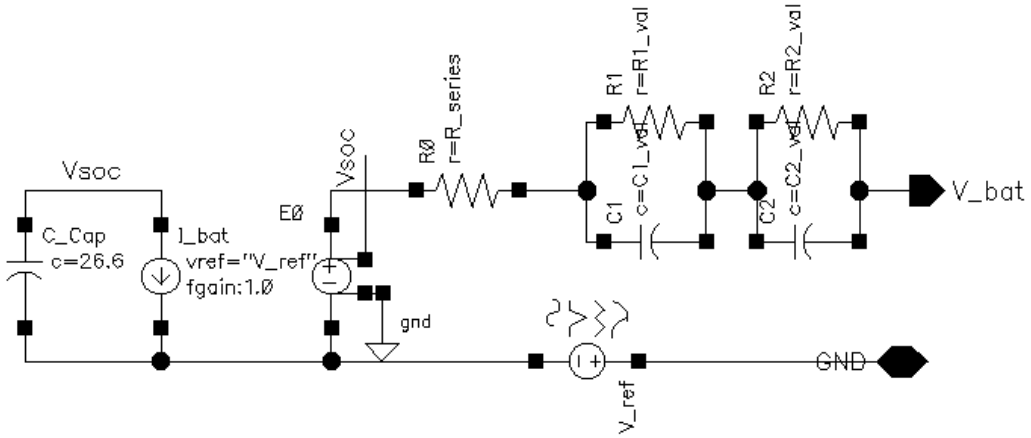

Figure 3.6: Equivalent model of the battery implemented in Virtuoso.

Two different schematic and cell views were created for each charge and discharge models. The difference between these two circuits lie essentially in the values of the circuit's parameters. To simplify the models, the parameters' variation with the SOC were not accounted for, so static values were adopted for each of the components. Average values were initially selected and continually fine-tuned based on the simulation results. The final selected values for the models' parameters are presented in table 3.4.

Table 3.4: Final parameters used in the equivalent circuit models.

Battery Model	R_series (Ω)	R1 (Ω)	C1 (F)	R2 (Ω)	C2 (F)
Charge	8	8	20	8	0.1
Discharge	8	8	0.1	8	20

A transient analysis was carried out, with the current source acting as a mean to pulse-charge and pulse-discharge the battery, depending on the value's polarity. An initial condition is specified to define the battery's initial SOC as 0 and 1 for the charge and discharge simulation, respectively. Figures 3.7 and 3.8 present the battery's terminal voltage for each of the two simulation conditions.

Analyzing the results, it can be seen that the models are able to replicate the terminal voltage's

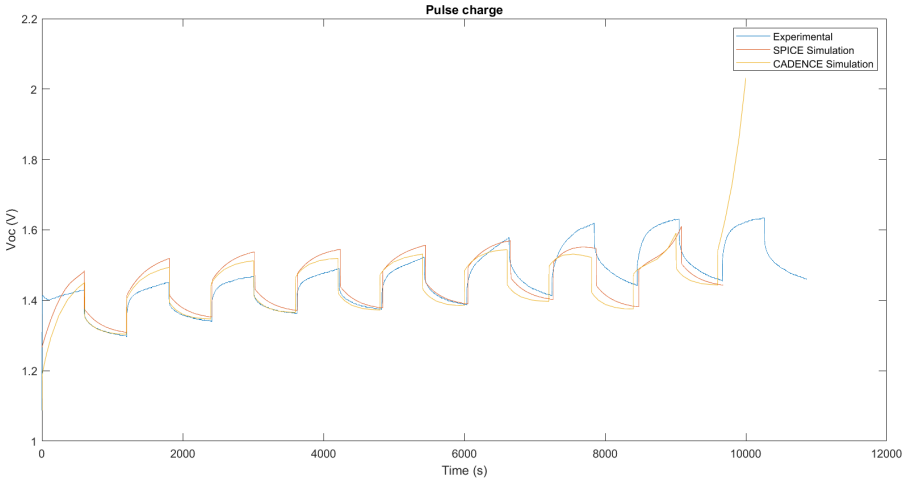

Figure 3.7: Terminal voltage during charge process: experimental vs simulation results.

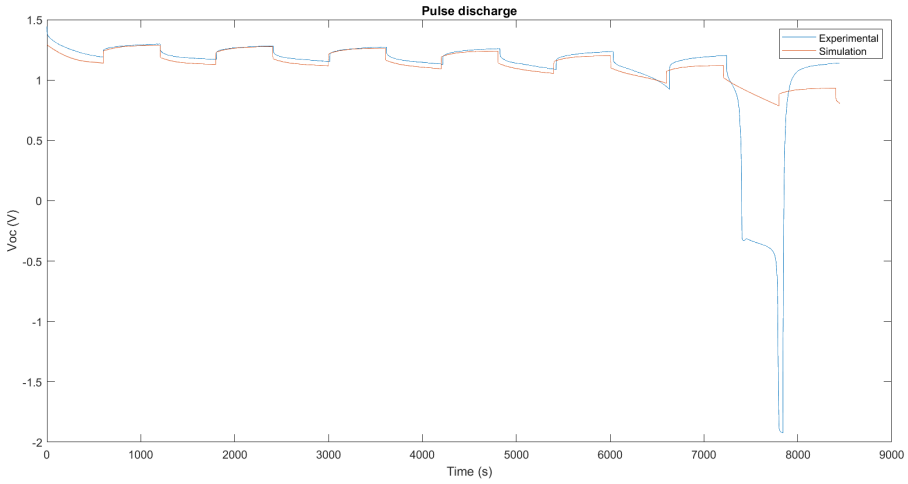

Figure 3.8: Terminal voltage during discharge process: experimental vs simulation results.

behaviour of the battery during the charge and discharge cycles, presenting a similar characteristic to the experimental results. There are some discrepancies in the position and exact values of the terminal voltage values. The delay of the experimental curve in regards to the simulation one is due to the discontinuity of the experimental equipment in the application of the current pulses. The parameter analyzer takes approximately one second to switch the current from zero to the specified value and this delay is not constant, making it burdensome to replicate the exact same behaviour in simulation. Furthermore, the disparity in the voltage values can be explained by the theoretical approximations made in the model extraction, namely the parameter's dependence on the temperature and cycle number, but most importantly, by the impossibility of replicating the parameter's variability with the battery's SOC.

In the experimental results, it is visible that the battery is discharged into reverse in the last current

pulse application. Efforts were made with different test configurations applied to different batteries, but preventing this behaviour posed a challenge due to the available lab equipment's limitation of measuring the battery's SOC. This behaviour however is not replicated in the model because it results from the battery's internal chemical functioning and cannot be fully described using the electrical equivalent model.

3.2 Photovoltaic Cells Characterization

3.2.1 Electrical Model for the PV Cells

For the purpose of this work, the *one diode five-parameter model* circuit, presented in figure 3.9, is adopted to represent the PV solar cell.

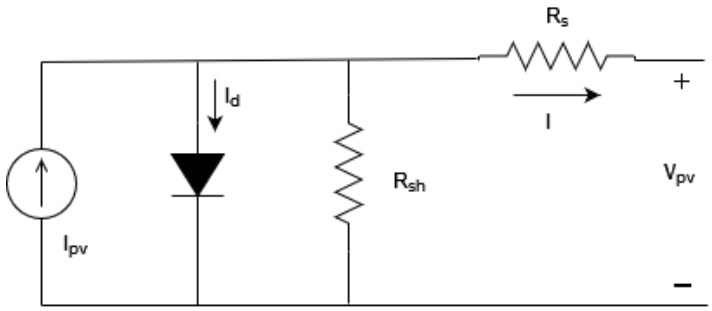

Figure 3.9: Equivalent circuit for a photovoltaic cell.

The behavior of a PV cell can be electrically described by a combination of both linear and non-linear components, as represented in figure 3.9. In this model, the ideal current source represents the current delivered by the solar cell in accordance with the incident radiation. In parallel with the source, there is an ideal diode that represents the cell p-n junction. In open-circuit a voltage V_{oc} appears at the PV cell's terminals. Two additional resistors are included, R_{sh} and R_s, to account for the electrical losses of the cell. If R_s is low enough for its value to be neglected (ideally it should be zero), when the terminals of the PV cell are short-circuited, there is no current through the diode and the short-circuit current I_{sc} corresponds to the current source's value. The PV cell's current can be described by the following expression 3.6.

$$I = I_{pv} - I_0 \left[\exp\left(\frac{V_{pv} + IR_s}{aV_T} \right) - 1 \right] - \frac{V_{pv} + IR_s}{R_{sh}} \tag{3.6}$$

where I_0 is the reverse saturation current of the diode, *a* is the ideality factor of the diode and V_T is the thermal voltage as described in 3.7

$$V_T = n\frac{kT}{q} \tag{3.7}$$

The thermal voltage V_T depends, in turn, on the number of cells in series *n*, on the Boltzman constant *k*, on the temperature *T* and on the electron charge *q*.

To sum up, in order to build a simulation-ready model of the PV cell, the following five parameters of the model must be obtained: R_{sh}, R_s, I_0, I_{pv} and a. The procedure carried out is described in the following sub-section.

3.2.2 Model extraction

The model's parameters can be computed based on the I-V characteristic of the PV cell, which is presented in figure 3.10. Using an extraction tool, this data was acquired from the datasheet and introduced in MATLAB.

The parameters of the equivalent model are not static, varying with the light intensity and with the wavelength of the incident radiation. For simplicity, the computation of these parameters is done considering the PV panel under full sun, which corresponds to an irradiance of 1000 W/m^2 (filled curve on figure 3.10).

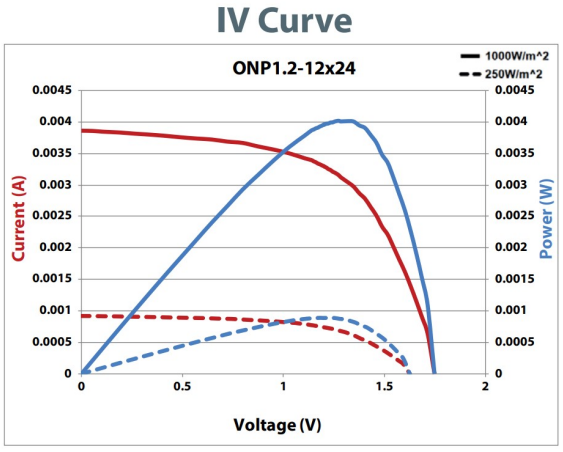

Figure 3.10: I-V Characteristic of PV cell from datasheet.

Adopting the method presented in [21], the following expressions are considered to compute the five parameters of the model.

$$\frac{aV_TV_{mp}(2I_{mp} - I_{sc})}{(V_{mp}I_{sc} + V_{oc}(I_{mp} - I_{sc}))(V_{mp} - I_{mp}R_s) - aV_T(V_{mp}I_{sc} - V_{oc}I_{mp})} = \exp\left(\frac{V_{mp} + I_{mp}R_s - V_{oc}}{aV_T}\right) \tag{3.8}$$

$$R_{sh} = \frac{(V_{mp} - I_{mp}R_s)(V_{mp} - R_s(I_{sc} - I_{mp}) - aV_T)}{(V_{mp} - I_{mp}R_s)(I_{sc} - I_{mp}) - aV_T I_{mp}} \tag{3.9}$$

$$I_0 = \frac{(R_{sh} + R_s)I_{sc} - V_{oc}}{R_{sh}\exp(\frac{V_{oc}}{aV_T})} \tag{3.10}$$

$$I_{pv} = \frac{R_{sh} + R_s}{R_{sh}} I_{sc} \tag{3.11}$$

By performing an initial estimate of the ideality factor *a*, it is possible to reduce the number of unknown variables from five to four, which makes the above expressions sufficient in determining the remaining parameters of the model. The ideality factor's value is normally bound to a small interval, typically between 1 and 1.5, for a single junction solar cell [21]. Selecting an initial value of 1.5 for parameter a, the following results were obtained for the model.

Table 3.5: Five-parameters obtained for the PV Cell's model

a	R_{sh} (Ω)	R_s (Ω)	I_0 (mA)	I_{pv} (mA)
1.5	1958	152	0	4

Table 3.6: Five-parameters obtained for the PV Cell's model

a	R_{sh} (Ω)	R_s (Ω)	I_0 (mA)	I_{pv} (mA)
1.5	2500	80	0	4

3.2.3 Model Simulation

With the results obtained analytically, a simulation-ready model of the PV cell was implemented in Virtuoso, as presented in figure 3.11.

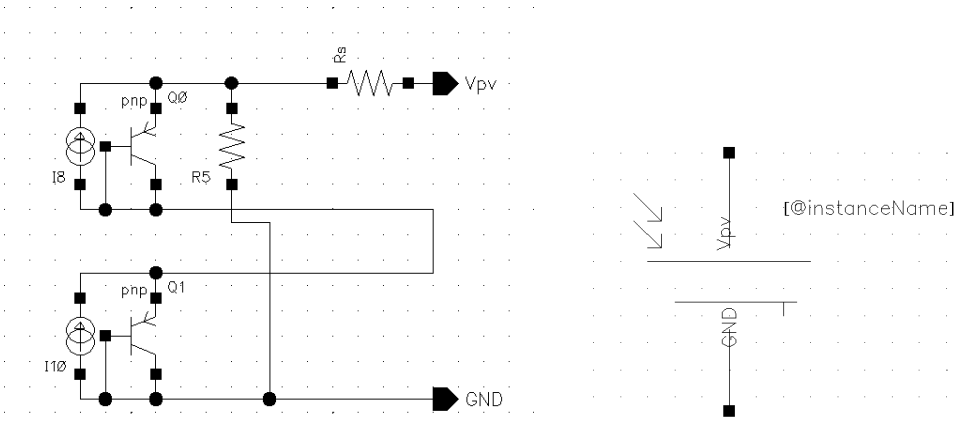

Figure 3.11: PV panel's model implemented in Virtuoso: schematic and symbol.

The model implemented represents two cells in series, which together compose the PV panel used in this project. A diode-connected PNP bipolar transistor is used to represent the model's diode. Using the estimate values from table 3.6 as a starting point, the model's parameters were continually fine-tuned to match the manufacturer's data. Figure 3.12 shows the I-V curve of the final model obtained, against the datasheet values.

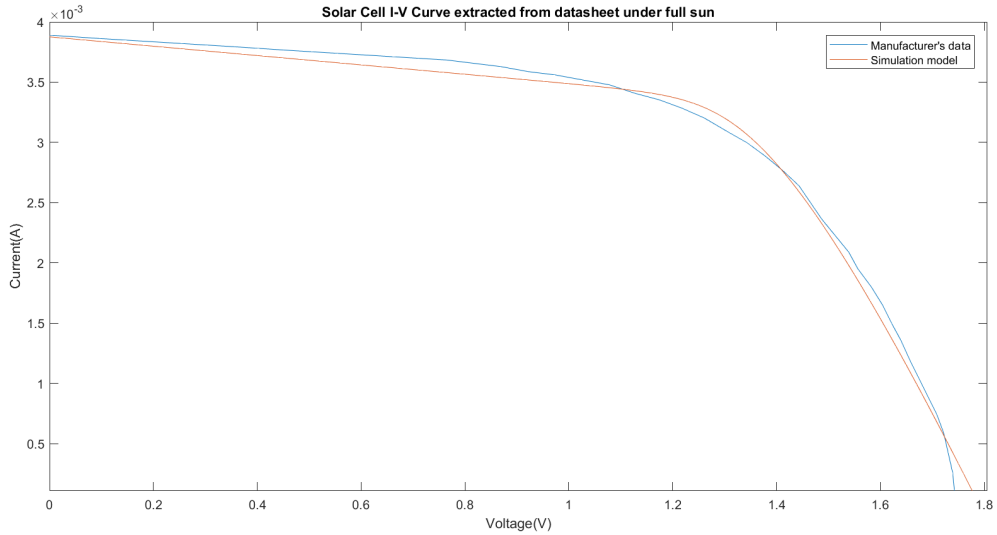

Figure 3.12: I-V Characteristic of the developed model vs the datasheet data.

4

Battery Charger System Design

Contents

4.1 System Architecture and Functional Blocks

The second part of this study consists on the development of a solar energy harvester circuit, that uses a photovoltaic module to supply a rechargeable NiMH battery.

The energy harvester system's primary target is to perform battery charging and battery management. For this system, the battery charging is performed through the direct charging method, in which the PV panel is directly connected to the battery through a switch. An alternative for this fully CMOS solution would be to include Switched capacitors (SC) or inductive DC-DC converters with MPPT tracking, which ensures that the PV panel is always working at maximum power point. However, these circuits would require a larger die-area to accommodate for the capacitors/inductors large sizes, it would require a higher operating frequency, which would greatly increase the power consumption of the system. Furthermore, the direct charging method can achieve even higher efficiency than other implementations that use DC-DC converters [22]. To increase the efficiency, it is advisable that the PV panel operates as close as possible to the maximum power point, and since in direct charging V_{pv} always follows V_{bat}, this can be ensured by choosing a PV module with a V_{MPP} close to the V_{EOC} of the battery. Considering that the V_{MPP} does not change significantly with the lighting conditions, the operation at Maximum power point (MPP) is secured throughout most of the charge and discharge process, the highest deviation corresponding to the situation where the battery is fully discharged and V_{bat} drops to approximately 1 V.

Figure 4.1 presents the proposed system's architecture, detailing the different functional blocks that compose the circuit.

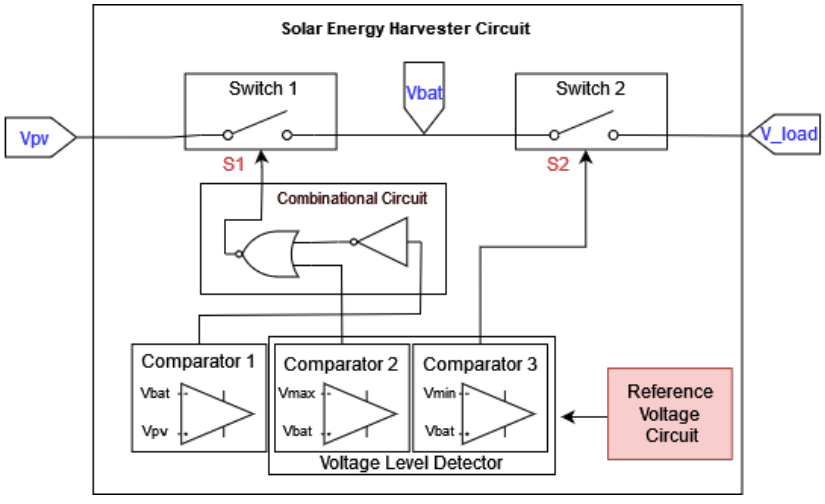

Figure 4.1: Solar Harvester and its functional blocks.

The system is essentially composed of switches, which allows to open/close the connection between the solar cells, the battery and the final load, comparator circuits which are used to monitor and compare

the different voltage levels existent in the system and a decision circuit which controls the charge/discharge process. A regular comparison is performed between the PV cells' and the battery's terminal voltages to assess when the charging process should take place. The switch S1 is controlled by the output of Comparator 1 and is only enabled when the PV cells' terminal voltage is higher than the battery's terminal voltage. When the PV cells' voltage is lower than the battery's voltage, the switch is turned off to ensure that the battery isn't discharged through the PV cells. The implemented battery management process consists on the verification that the battery remains within the specified V_{min} and V_{max} voltages during charge and discharge, to prevent overcharge and deep-discharge, which reduces battery lifetime and its overall performance. This is accomplished by a Voltage Level Detector Circuit that continually compares the battery's terminal voltage with the defined EOC and EOD voltage levels, and decides whether the charge/discharge should be interrupted. According to the datasheet, the V_{EOC} and V_{EOD} voltages for this battery are approximately 1.5 V and 0.9 V, respectively. For the purpose of this work, the minimum battery voltage for the system's operation will be assumed as 1 V, so the defined limits for the system will be V_{min} = 1 V and V_{max} = 1.5 V. At last, a simple combinational circuit is used to manage the system, properly verifying all the aforementioned conditions and controlling the selection of the switches.

Figure 4.2 presents an illustration of the different operating conditions, along with the expected states and outputs of some reference signals for each situation.

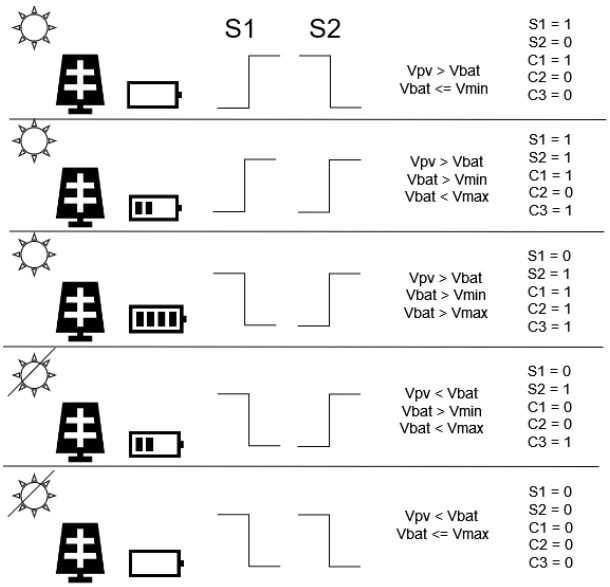

Figure 4.2: Expected system's operation under different conditions.

The system's operation is affected primarily by the available light intensity and the battery's SOC. In the situations where there is enough ambient light to charge the battery, switch S1 will be on, as long as the battery does not exceed the maximum specified voltage. The state of switch S2 is affected solely

by the battery's voltage: if the battery has enough charge and is not below V_{min} then S2 should be on, otherwise the switch is turned off to disconnect the battery from the final load. The analysis of the different comparator's outputs and how they affect the control signals for the switches is presented in more detail in the upcoming sections.

The system's schematic implemented in Virtuoso is presented in figure 4.3.

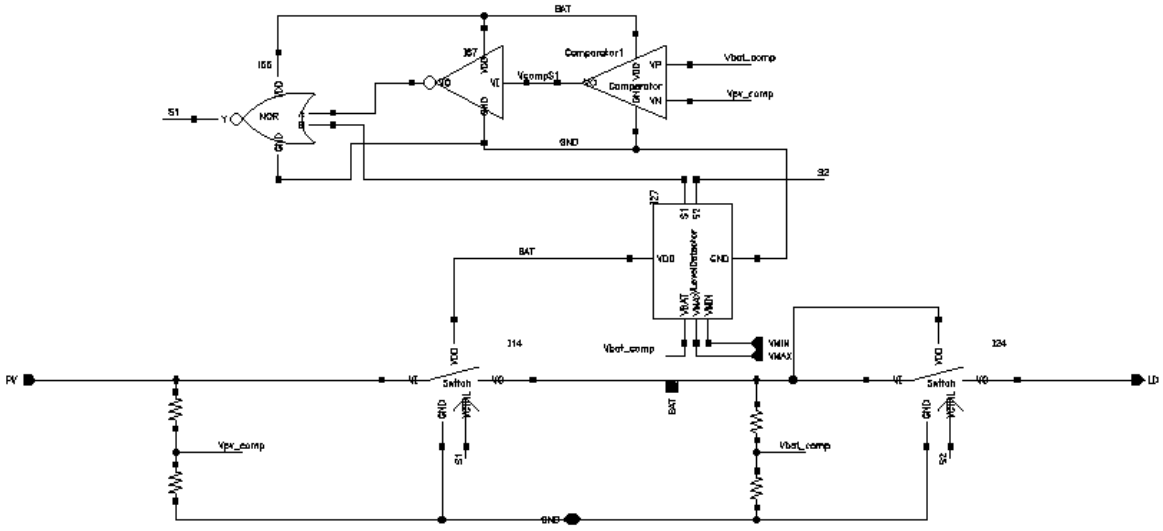

Figure 4.3: System's schematic.

One thing to note is the presence of the two resistor pairs connected to the input and the battery output of the system. These resistors are used to lower the voltage levels of Vpv and Vbat to be used in the comparator circuits. Assuming that the reference voltages that represent V_{max} and V_{min} will be originated by a BGR circuit, and bearing in mind that the whole system is supplied by the battery, there is a need to ensure that these reference voltages can be accurately generated even in the situations where Vbat drops to 1 V. Hence, the safest approach to safegaurd the correct operation of the circuit is to define voltage references that can be produced from a 1 V supply voltage. For this reason, the selected reference voltages are V_{max}=1.5/2 = 750 mV and V_{min} =1/2 = 500 mV, which compels the use of two equal resistors in series. In order to decrease power consumption, it is desirable that these resistor values are as high as possible, to lower the current that is dissipated through them. However, there is a trade-off between the current loss and the layout area that should be taken into account, since higher resistors are also bigger in size. In this case, four high resistance polysilicon resistors of 35 kΩ were used for this purpose.

4.2 Comparator

Considering the low speed operation necessity of the solar harvester, a simple two-stage self-biased Operational Amplifier (OpAmp) is used as a comparator, in an open-loop configuration. The implemented circuit is presented in figure 4.4.

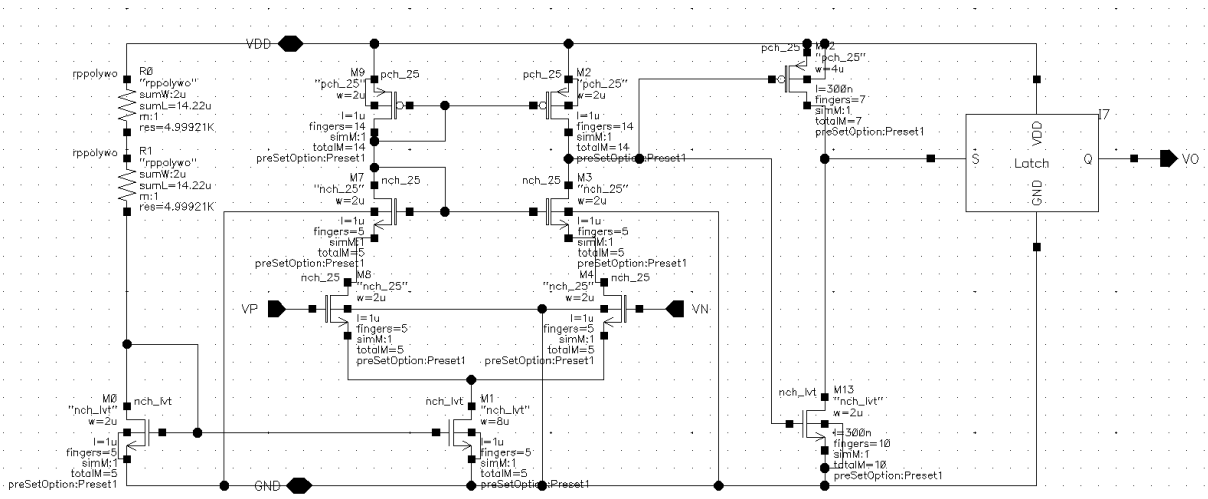

Figure 4.4: Comparator schematic.

This topology uses an N-channel metal-oxide semiconductor (NMOS) differential pair with a cascode current mirror that improves the output resistance of the OpAmp. Two high resistance polysilicon resistors in series are used for biasing, as a means to optimize layout area. The comparator was designed with a push-pull output configuration and the current in the first branch is approximately 20 µA. A simple latch is included at the output to improve the quality of the signal for digital control.

In figure 4.5, the output of the comparator is shown, when comparing the voltages from the PV cells and the battery, using the own battery as bias. In this simulation Vbat is connected to the positive input and Vpv is connected to the negative input.

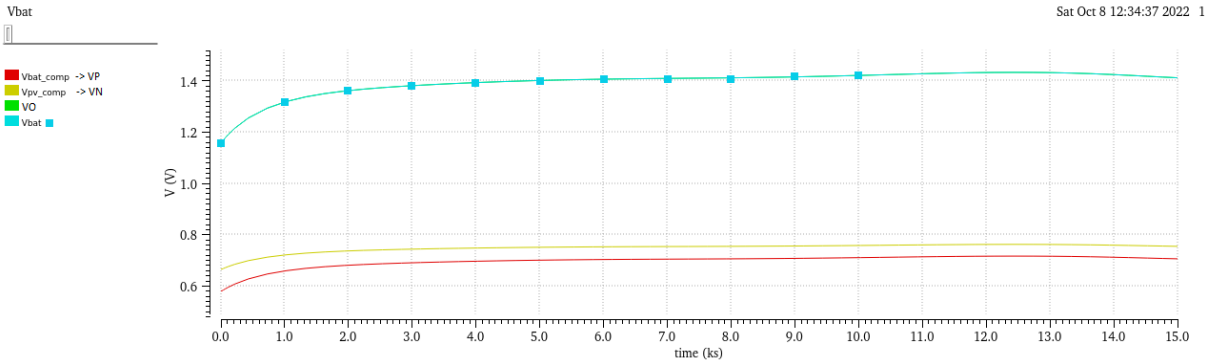

Figure 4.5: Comparator's simulation results.

Since this is a two-stage amplifier, the comparator also acts as an inverter, meaning that the output will be high when the positive input is lower than the negative input. For the case depicted above, the PV cells' voltage is higher than the battery's voltage, therefore the output of the Comparator is high, as expected, following exactly the battery's terminal voltage.

Table 4.1 summarizes the sizes and values used for the different components of the comparator.

Table 4.1: Comparator's components' sizes and values.

Transistor	W (m)	L (m)	Nº fingers	Transistor	W (m)	L (m)	Nº fingers
M0	2 u	1 u	5	M5	2 u	1 u	15
M1	8 u	1 u	5	M6	2 u	1 u	5
M2	2 u	1 u	14	M7	2 u	1 u	5
M3	2 u	1 u	5	M8	4 u	300 n	7
M4	2 u	1 u	5	M9	2 u	300 n	10

Bias resistor	2 u	28.44 u	10 kΩ

4.3 Voltage Level Detector

The Voltage Level Detector circuit compares the battery's voltage with V_{min} and V_{max} voltages to oversee that V_{bat} does not go beyond these values. The reference voltages that should be generated by a BGR, are each compared with V_{bat} through the use of two individual comparators, both identical to the one previously presented. The schematic of this block is presented in figure 4.6.

The battery's datasheet specifies the V_{EOC} and V_{EOD} voltages as approximately 1.5 V and 0.9 V, respectively. For the purpose of this work, we will consider the minimum battery voltage for the system operation as 1 V. Considering that the whole system will be supplied by the NiMH battery, the supply voltage becomes a limitation in the design of the BGR, due to the inability to generate reference voltages that are higher than the supply voltage. For this matter, the reference voltages selected to be generated were 0.75 V and 0.5 V to represent both V_{EOC} and V_{EOD} , respectively. By using a voltage divider with resistors in series, an accurate comparison is achieved between the battery's terminal voltage and the selectedthreshold voltages.

The behavior of this block for the case when both switches are on is presented in figure 4.7.

4.4 Combinational Circuit

The control unit of this circuit essentially consists on the management of the two switches, which can be either ON or OFF, depending on the set of conditions specified for each case.

As previously mentioned, S1 must be ON only if the following two conditions are met: if the solar

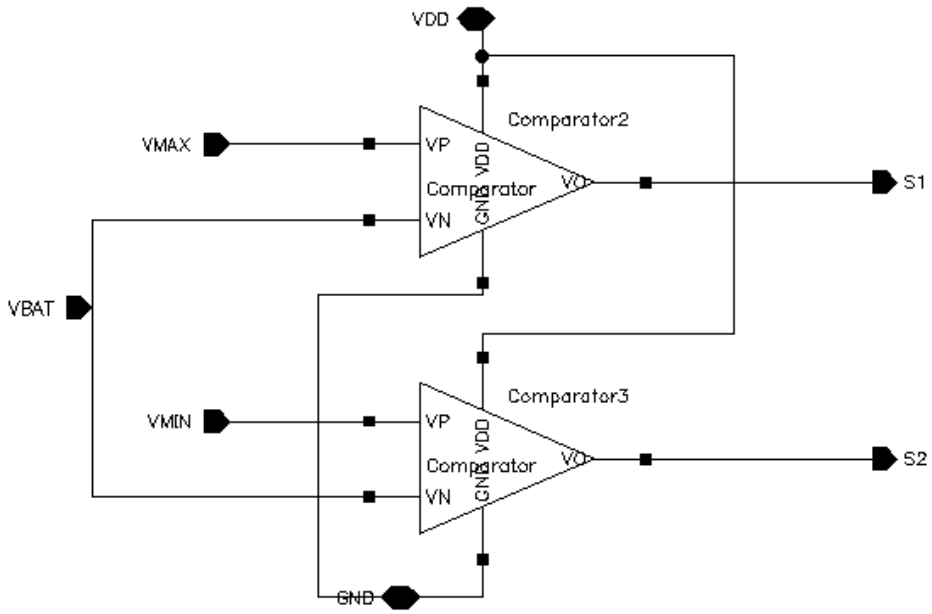

Figure 4.6: Voltage Level Detector schematic.

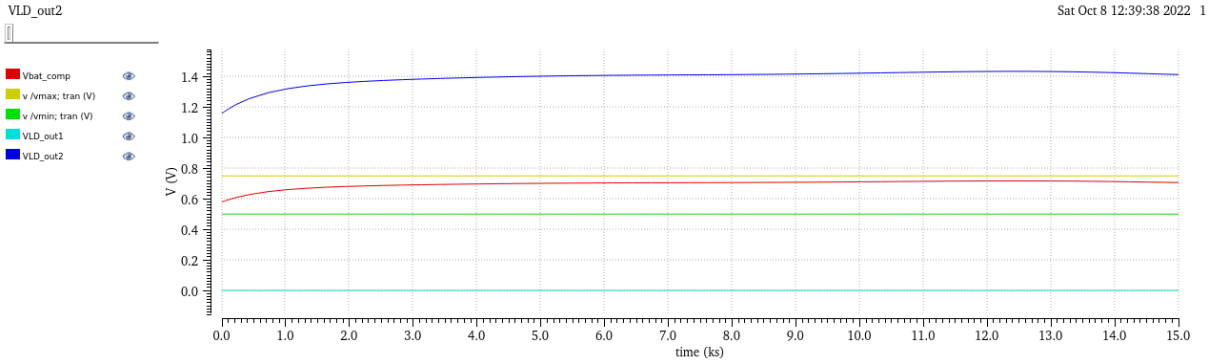

Figure 4.7: Voltage Level Detector output when both switches are on.

cell's terminal voltage is higher than the battery's voltage, so that there is no discharge through the cell, and while the battery's voltage is less than the EOC terminal voltage. As for S2, which controls the battery's charge of the load, it should be ON only if the battery's voltage is higher than the specified EOD voltage of 1 V. Due to the simplicity of the system, a simple combinational circuit is used to verify these statements, based on the truth-table presented in Table 4.2. The signals C1, C2 and C3 correspond respectively to the output of the first, second and third comparators, specified on figure 4.1.

From the above table, the following logic relations can be obtained:

$$S1 = C1 \cdot \overline{C2} \tag{4.1}$$

Table 4.2: Truth-table for the combinational circuit.

C1	C2	C3	S1	S2
0	0	0	0	0
0	0	1	0	1
0	1	0	0	0
0	1	1	0	1
1	0	0	1	0
1	0	1	1	1
1	1	0	0	0
1	1	1	0	1

$$S2 = C3$$

By applying boolean algebra to 4.1, the combinational logic for S1 can be further simplified to

$$S1 = \overline{\overline{C1} \oplus C2} \tag{4.2}$$

which corresponds to the final circuit used in the system. Figure 4.8 presents the gates used to control S1.

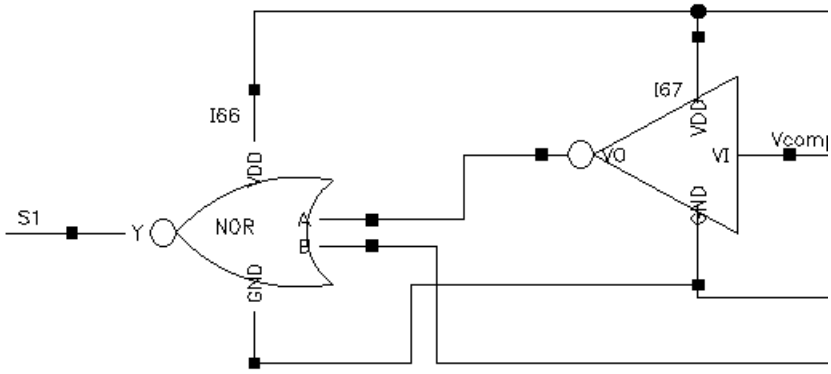

Figure 4.8: Logic gates used to control S1.

The inverter is used to make C1's complement, that is, to invert the output signal of comparator 1. The resulting signal is applied to a NOR gate, along with the output of comparator 3, to obtain the final control signal for S1.

4.5 Switches

In this system, the switches are used to control when the PV panel is connected to charge the battery and when the battery is connected to feed the load. Since a direct charging method is employed, the switch should be large enough so that the voltage drop between Vpv and Vbat is negligible. When the switch is turned ON, Vpv will follow Vbat and charge the battery.

For this purpose, a transmission gate is used for the switch, as presented in figure 4.9.

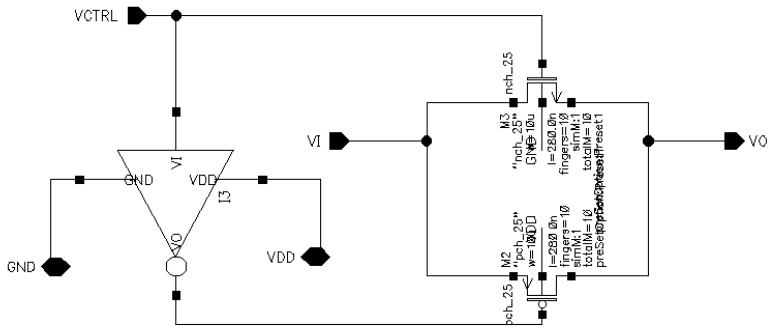

Figure 4.9: Switch schematic.

The transmission gate consists of one NMOS transistor in parallel with a P-channel metal-oxide semiconductor (PMOS) transistor. The principle of this circuit is to bias the transistors with complementary control signals to ensure that they are both either ON or OFF simultaneously. When the control signal is high, both transistors will be ON and the switch will be closed; when the control signal is low, both transistors will be OFF and the switch will be open with no current flowing through it, ideally.

The advantage of using a transmission gate instead of using a simple NMOS or PMOS switch is because both transistors will be conducting when the switch is ON and the input will always be passed to the output for both situations, either through one transistor or the other.

Figure 4.11 presents a simple example of the functioning of this switch. The testbench used is presented in Figure 4.10.

As illustrated in the image, the state of the switch is controlled by the input signal V_{ctrl}. When V_{ctrl} is high, the switch is ON, presenting a voltage drop as low as 702 μV and a current of approximately 12 μA. When the control signal is low, the switch is open, with a current as low as 60 pA. With these values an estimate can be done of the ON resistance value of the switch as shown in 4.3.

$$R_{on} = \frac{V_{on}}{I_{on}} = \frac{703\,\mu V}{12\,\mu A} \approx 59\,\Omega \tag{4.3}$$

The ON resistance should be as low as possible to simulate a short-circuit and the current when the switch is OFF should be ideally zero to simulate an open-circuit. The OFF current, which can be seen in

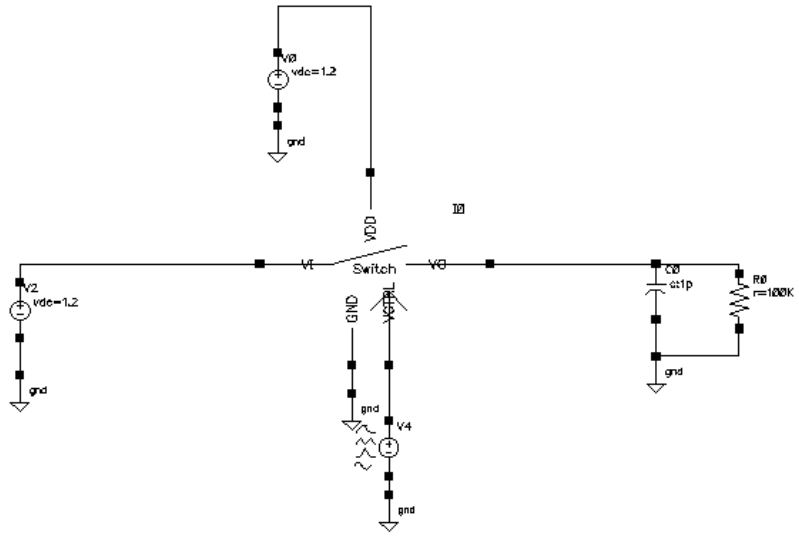

Figure 4.10: Switch testbench.

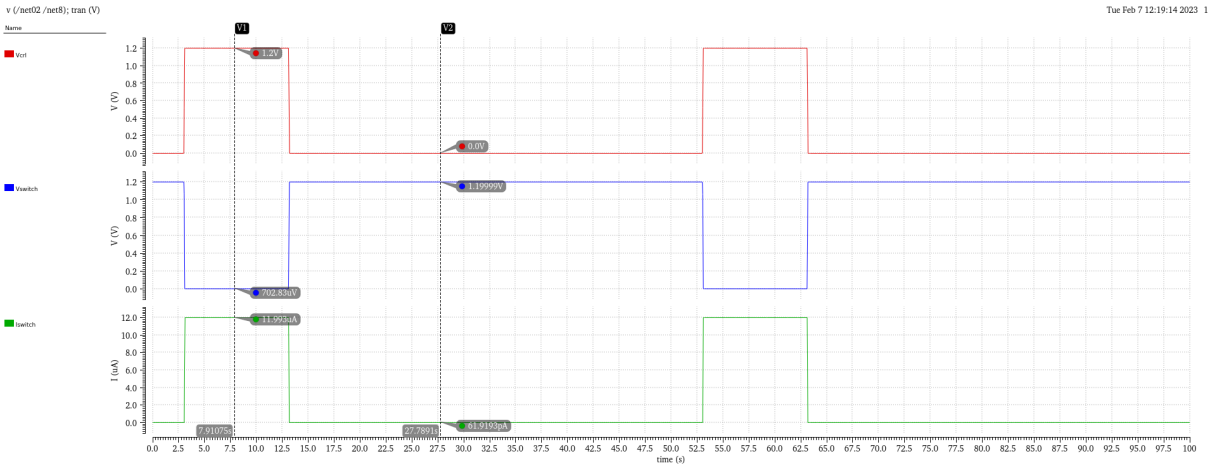

Figure 4.11: Outputs obtained for the switch operation: red - switch's control signal, blue - voltage drop across the switch, green - current across the switch.

the figure, is around 62 pA. As such, these results are suitable for the functioning of the system.

4.6 System Layout

After designing and simulating the complete circuit, the full layout of the system was developed, as presented in figures 4.12, 4.14 and 4.13.

The layout was executed taking into account the design rules of the technology, while simultaneously applying techniques with the end goal of reducing parasitic effects and optimizing layout space. As previously mentioned, *Rppoly* resistors were used, since these present the highest resistance per unit

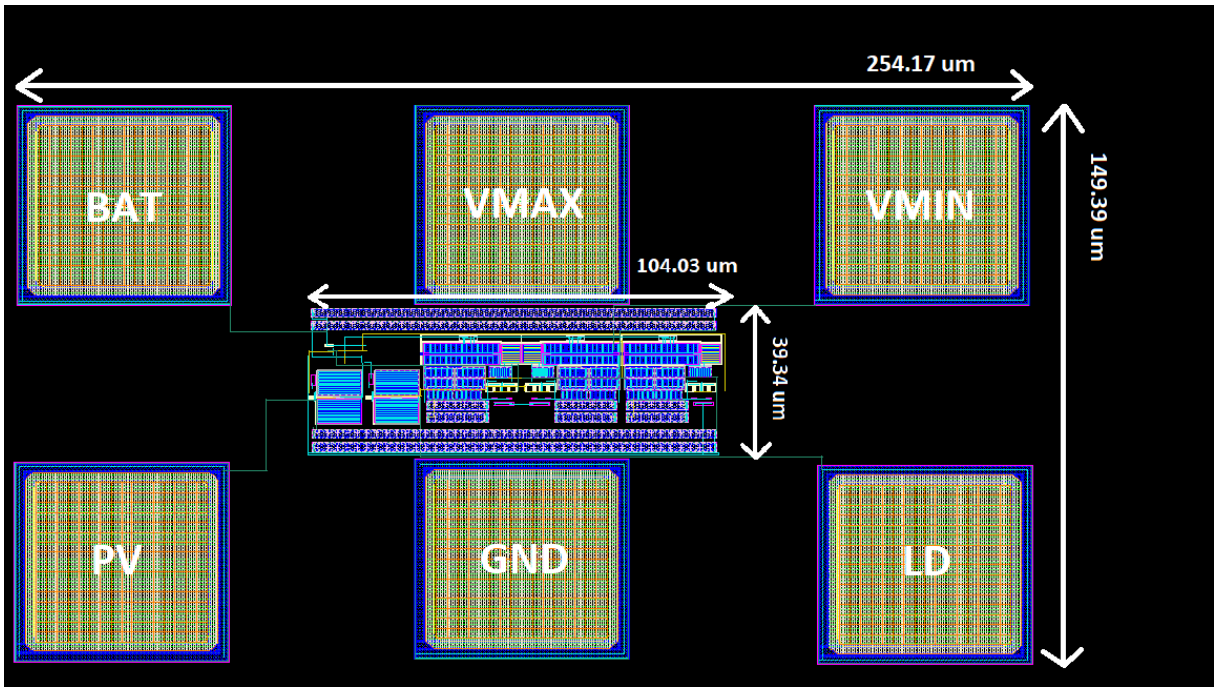

Figure 4.12: Full system layout including pads.

Figure 4.13: System layout with functional blocks.

area of the technology, making it possible to obtain the desired resistance values in less area. These resistors are employed in a series configuration to optimize layout area. Three metal layers are used, at most, to perform all the connections in the system. The final layout resulted in an area of 254.17 x 149.39 μm^2, including the pads. Table 4.3 presents in detail the die area occupied by each of the common blocks that compose the system.

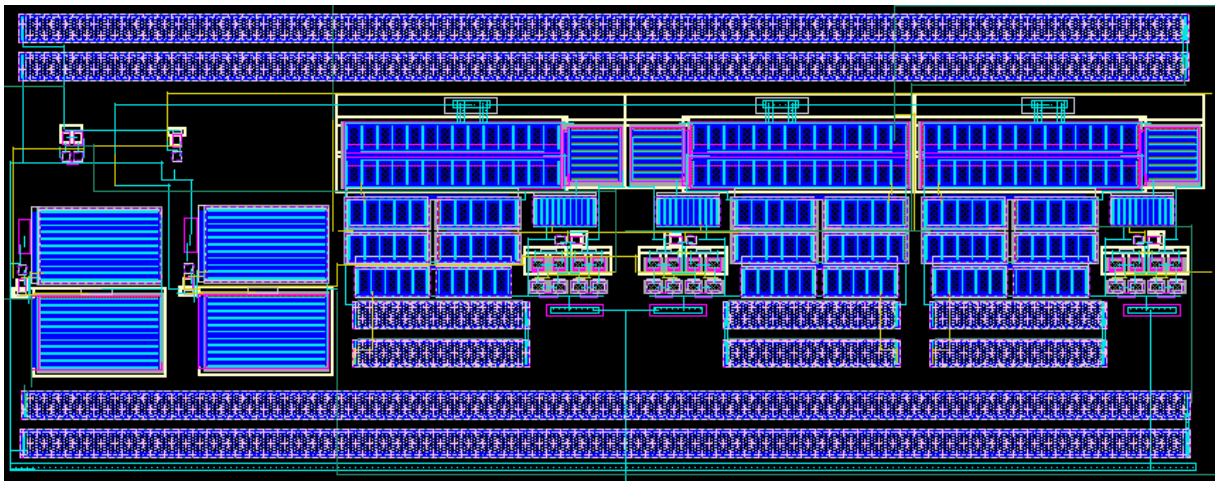

Figure 4.14: System layout in detail.

Table 4.3: Die area of functional blocks and components

Functional Block	**Die Area (μm)^2**
Inverter	4.18
NOR gate	7.25
Switch	192.79
Comparator	588.75
Voltage Level Detector	1181.50
Voltage feedback resistor	1140
Total occupied area	**37970.46**

4.7 Dispersion in the Voltage References

As previously stated, the threshold voltages used to monitor the EOC and EOD levels of the battery are meant to be generated by an on-chip voltage reference circuit. Since the entire system is fed by the battery and the battery's voltage is variable over time, it is important to contemplate how these fluctuations can impact the reference voltages and the overall operation of the system. To account for this effect, a consideration had to be made on how these reference voltages vary with the bias voltage.

After a detailed researched on the already existent voltage reference circuits in 65 nm CMOS technology that more closely match the requirements for the reference values needed in the system, the circuits presented in [23] are considered. Examining the MOS circuit presented, it can be confirmed that the line regulation, defined by the expression in 4.4, is 3.8%, for an approximate reference voltage of 680 mV.

$$LR = \frac{\Delta V_{ref}}{V_{ref}} \times \frac{1}{\Delta V_{DD}} \times 100 \tag{4.4}$$

Considering the reference voltage dispersion that might occur, the bias voltage and the reference voltages can be described as

$$V_{DD} = V_{DD0} + \Delta V_{DD} \tag{4.5}$$

$$V_{ref} = V_{ref0} + \Delta V_{ref} \tag{4.6}$$

where, for this system, V_{DD} corresponds to V_{bat}. Substituting 4.4 in 4.6 and applying this variation to our reference values, the following relation can be obtained for the reference voltages:

$$V_{min} = 499.62m + 0.38m \times V_{bat}\ [V] \tag{4.7}$$

$$V_{max} = 749.43m + 0.38m \times V_{bat}\ [V] \tag{4.8}$$

When it comes to temperature, it is seen in simulation that for one of the chips, the temperature coefficient is 157 ppm/ºC. This is the value that will be considered in our system.

To simulate the system with these variable reference voltages, the two ideal sources present in figure 5.1 were replaced by voltage dependent voltage sources, following the variations described in 4.7 and 4.8, and the temperature coefficient of 157 ppm/ºC. These sources and their respective setup are presented in figures 4.15 and 4.16.

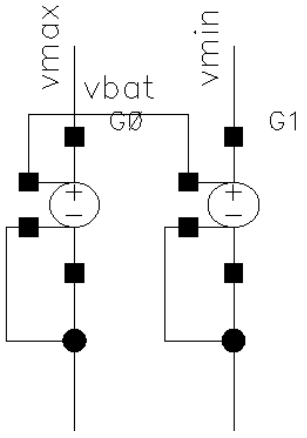

Figure 4.15: Voltage dependent voltage sources used to emulate BGR variations.

Max Coefficient Number	1
Poly Coeff 0	749.43m
Poly Coeff 1	0.38m
Gain	1.0
Multiplier	
Smoothing Factor	
Maximum Output Voltage	
Minimum Output Voltage	
Temperature coefficient 1	157u

Max Coefficient Number	1
Poly Coeff 0	499.62m
Poly Coeff 1	0.38m
Gain	1.0
Multiplier	
Smoothing Factor	
Maximum Output Voltage	
Minimum Output Voltage	
Temperature coefficient 1	157u

Figure 4.16: Setup values for the voltage dependent voltage sources.

Figure 4.17 graphically presents the reference voltages' variation with temperature.

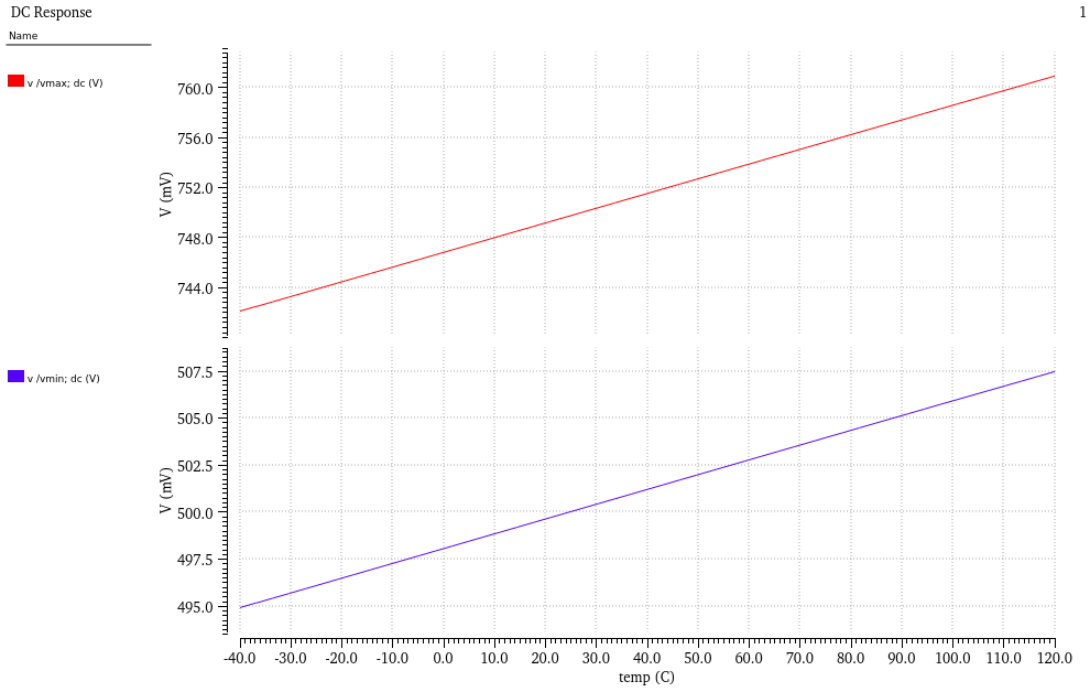

Figure 4.17: Reference voltages variations.

Despite being stated in [23] that the temperature variation observed is only valid from 40 ºC to 125 ºC, in this analysis, the same variation was adopted throughout all the considered temperature range. An approximate difference of 20 mV can be observed between the maximum and minimum values for V_{max}, for example, which correspond to the extremes temperature of -40ºC and 125 ºC. This translates to a relative deviation of 26.7% for both reference voltages.

In our analysis, the reference's voltage dependency on V_{bat} is of special importance, since the battery serves as the bias voltage for the whole system and its value can be highly variable. This variation is assessed on figure 4.18.

From these results, it is possible to confirm that the reference's variation with V_{bat} is indeed low,

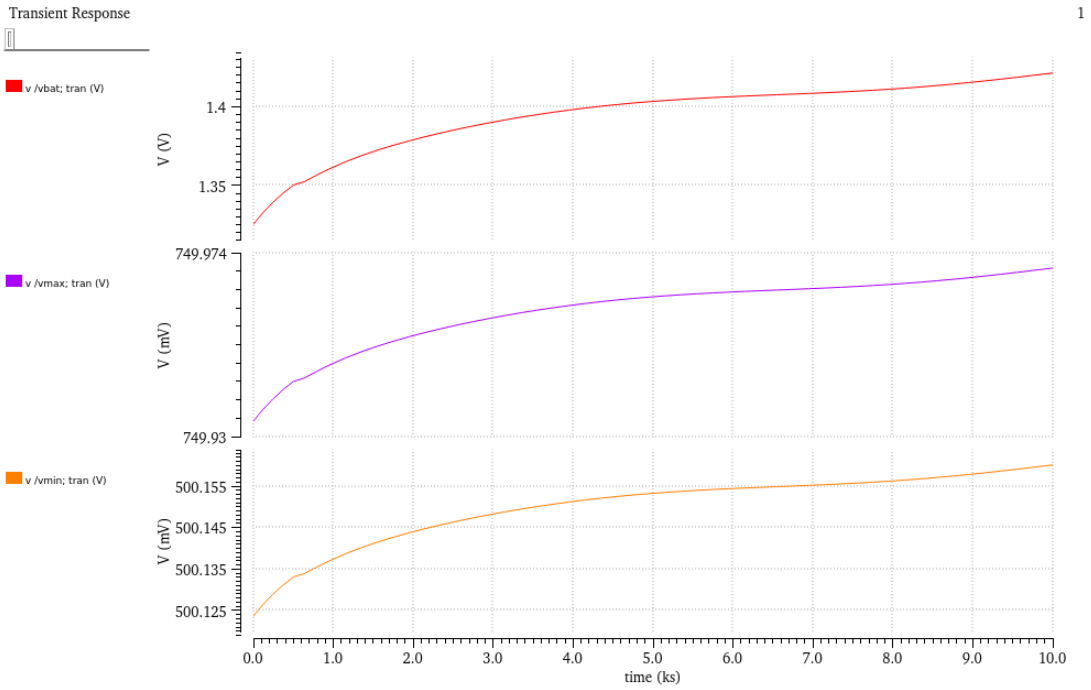

Figure 4.18: Reference voltages variations.

varying 0.04 mV for a V_{bat} variation of 10 mV, which is a very satisfactory result.

5

Final Results

Contents

In this chapter the final system is tested in simulation for different operation conditions. The results obtained are presented and discussed and the system's validation is performed based on these results.

5.1 System Simulation in Nominal Conditions

After successfully performing DRC, LVS and extraction, the extracted view was simulated in nominal conditions (T = 300 K), to test the final operation of the system.

Figure 5.1 presents the testbench used. The models previously presented for the PV panel and the battery are used in this simulation to achieve a more accurate indication of what would be the real operation of the system. Different setups were used to test the system for the different conditions that were considered in the design stage.

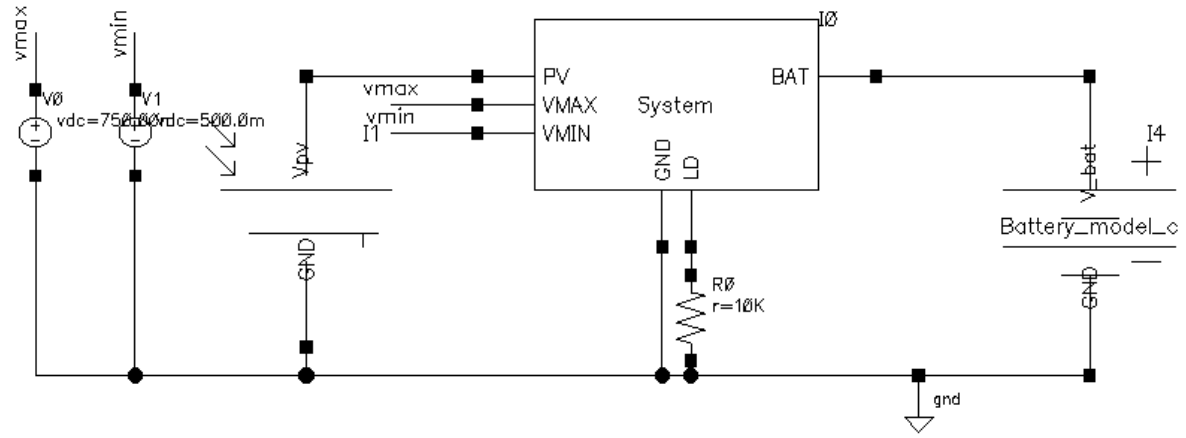

Figure 5.1: System testbech.

The first test that was carried out considers the PV panel under maximum light intensity and the battery deeply discharged. For this case, it is expected that S1 is ON, with the PV panel charging the battery, and that S2 switch is OFF, since the battery does not have enough energy to feed the load. Figure 5.2 presents the relevant signals obtained for this first setup.

In this scenario, the initial SOC is defined as -0.1 V, to ensure that the battery's initial voltage is below the EOD voltage, representing a deeply discharged state. As expected, S2 is OFF in the initial stage. S1 is ON, since V_{pv} is higher than V_{bat}. The initial charging current is higher, corresponding to the rapid voltage increase that takes place when the charging process is initiated, as previously studied in Chapter 2, when the battery's charging process was analyzed. After this initial stage, the charging current stabilizes to approximately 1.7 mA. S2 is turned ON exactly when the battery's voltage reaches 1 V, which happens after approximately 8 minutes. From this moment on, the system feeds the load with

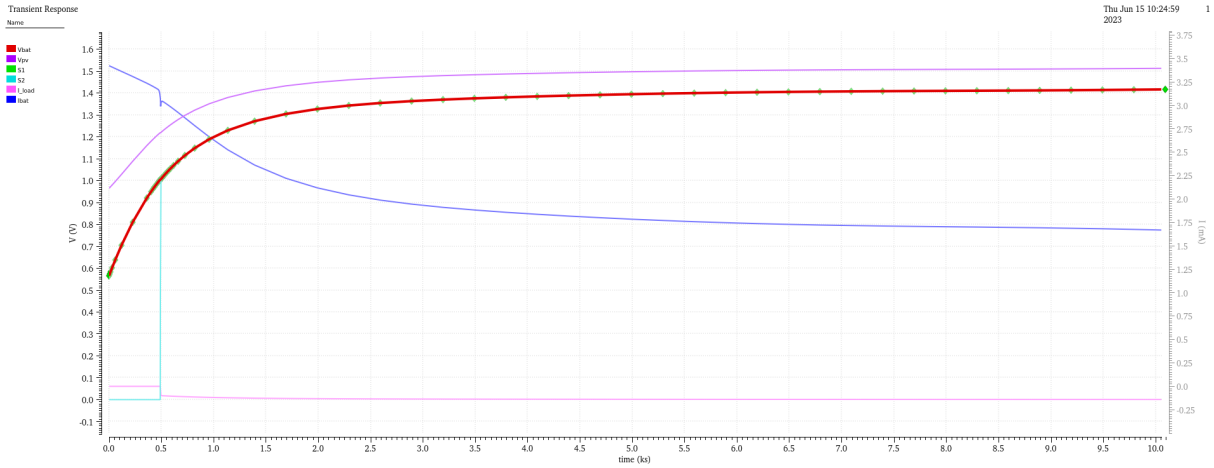

Figure 5.2: Results for nominal simulation for the first setup test: initial SOC = -0.1 V, R_{load} = 10 kΩ and Ipv = 4 mA.

a constant current of 140 μ A, while the battery is continually charged by the PV panel.

The second test considers when there is no available light to power the PV cell, but the battery is half charged. The results for this scenario is presented in 5.3.

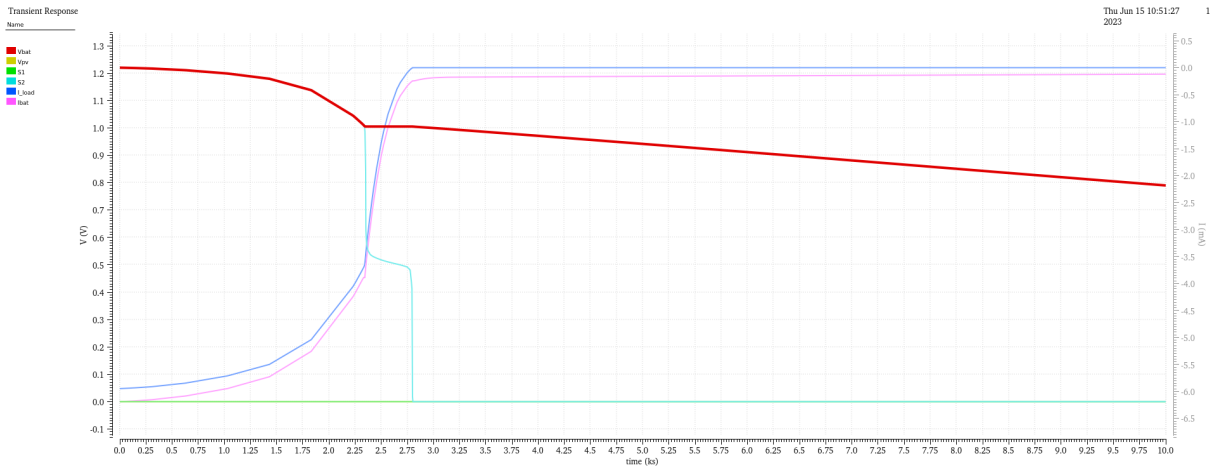

Figure 5.3: Results for nominal simulation for the second setup test: initial SOC = 0.5 V, R_{load} = 100 Ω and Ipv = 0.

For this case, an initial SOC of 0.5 V was defined, which corresponds to an initial V_{bat} of approximately 1.2 V. S1 is OFF since the PV panel does not generate any voltage. A load of 100 Ω was used to optimize simulation time while ensuring that the battery reaches the EOD voltage. In the initial stage, the battery is used to feed the load with a current of roughly 5.9 mA. Around 1.5 mA the battery is used to operate the system, which totals an output discharge current in the vicinity of -6.12 mA. The battery is capable of supplying this current up to around 25 minutes, after which the considered EOD voltage is achieved, and S2 is turned OFF.

Table 5.1 presents a summary of the setup tests that were used, specifying the initial conditions

considered for each case (first four columns), as well as the respective observed outputs.

Table 5.1: Summary of setup tests performed and outputs obtained.

Setup test	SOC_0 (V)	I_{pv0} (mA)	R_L (Ω)	S1	S2	I_{bat} (A)	I_{load} (A)
Test 1	-0.1	4	10 k	1	0	≈ 3 m	0
				1	1	≈ 1.7 m	≈ 140 µ
Test 2	0.5	0	100	0	1	≈ –6 m	≈ 5.9 m
				0	0	≈ –130 µ	100 n

5.1.1 Operation Under Different Lightning Conditions

In the analyzes presented so far it was only considered the PV panel in two different conditions, which correspond to the cells under full light intensity and under no light. However, other scenarios should also be acknowledged to better evaluate the system's performance under different circumstances, since more often than not, the environmental conditions do not correspond to the ideal scenario. In order to do so, a parametric analysis was carried out, with different I_{pv} values to emulate these different lightning conditions. The results obtained are presented in Figures 5.4 and 5.5.

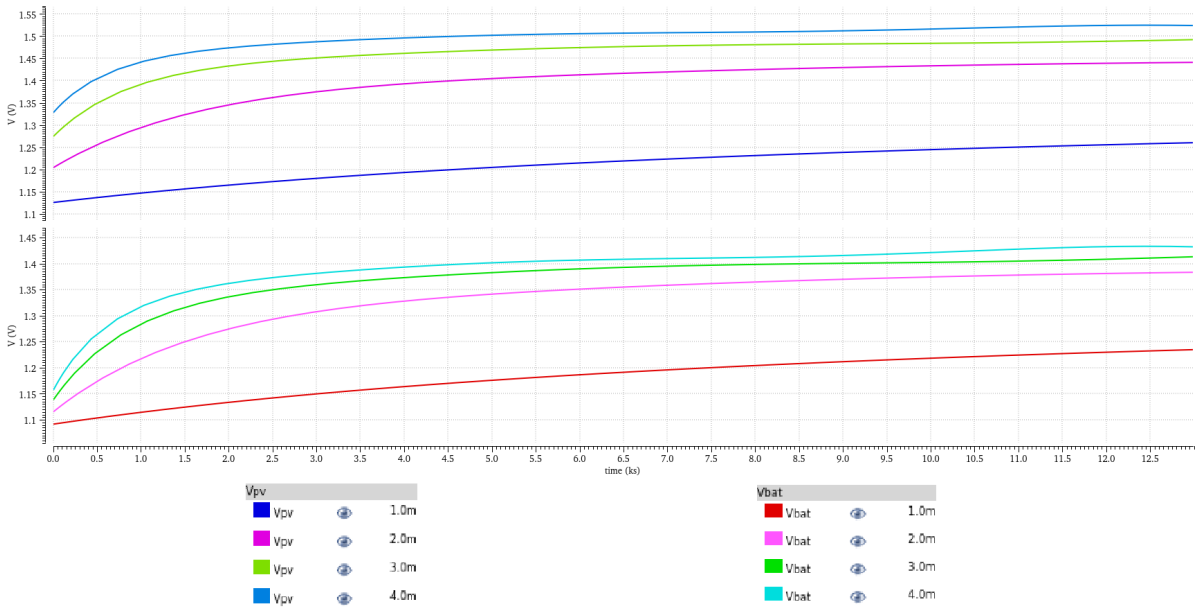

Figure 5.4: Vpv (signals above) and Vbat (signals below) under different lightning conditions.

As expected, the charging rate is proportional to the charging current, which in this case is the current made available by the PV panel. This dependence however is not linear. With 1 mA the battery charges more slowly than with 2 mA, but the charging curve with 3 mA and 4 mA do not present a drastic variation. Table 5.2 presents a summary of some charging characteristics and how these vary with the input solar cells' current.

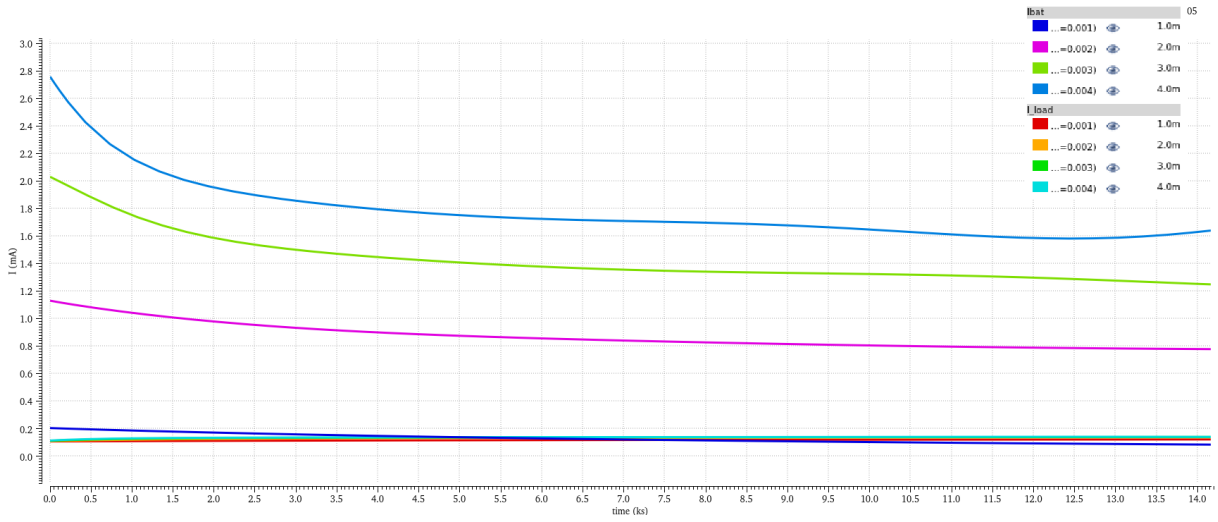

Figure 5.5: I_{bat} and I_{load} currents under different lightning conditions.

Table 5.2: Charging characteristics under different lightning conditions.

Ipv (A)	t (Vbat=Vn)	I (t=10000 s) (A)
1 m	3.9 h	158.9 µ
2 m	45.9 mn	825.8 µ
3 m	24.5 mn	1.33 m
4 m	16.6 mn	1.67 m

In the table above, the second column corresponds to the time that it takes for the battery to reach its nominal voltage of 1.2 V. The third column shows the stable charging current, using as reference the timestamp of 10000 s. These results are an indication that the system can still operate with reasonable performance, even when the PV cells are under a lower light intensity. Naturally, the higher the charging current, the faster the battery will charge to a desired voltage level.

Figures 5.6 a) and b) present the daily irradiance in Portugal, for a typical day in the months of December and July, respectively. Analyzing the data, one can see that the global incident irradiance available exceeds 200 W/m^2 during at least 8 hours on a winter day and for at least 11 hours on a summer day. Considering the V/I characteristic of the solar cells, presented in figure 3.10, the current corresponding to the situation in which the cells are under 1/4 sun (200 W/m^2) are approximately 1 mA. Based on the obtained results, with 1 mA, the battery takes almost 4 hours to reach the nominal voltage, which can still be assured for a winter day. Depending on the application and on the final load value, this charging rate can be more or less desirable, but the current available is sufficient to charge the battery, even if under trickle charging conditions.

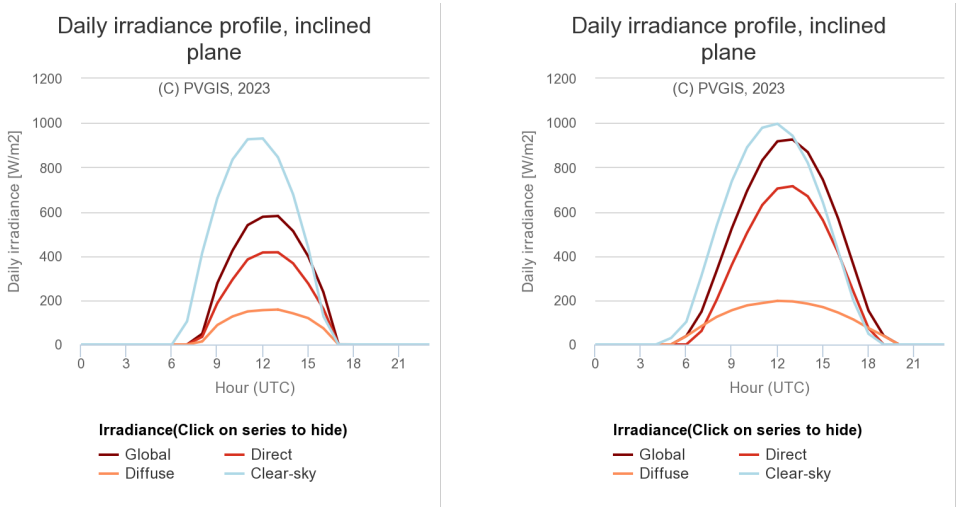

Figure 5.6: Daily irradiance in Portugal: a) December; b) July.

5.1.2 Operation with Different Loads

Figure 5.7 presents the battery's discharge for different load values. A sweep was performed in the output resistor and a transient simulation was conducted with the PV cells under full sun and an initial SOC of 10% for the battery.

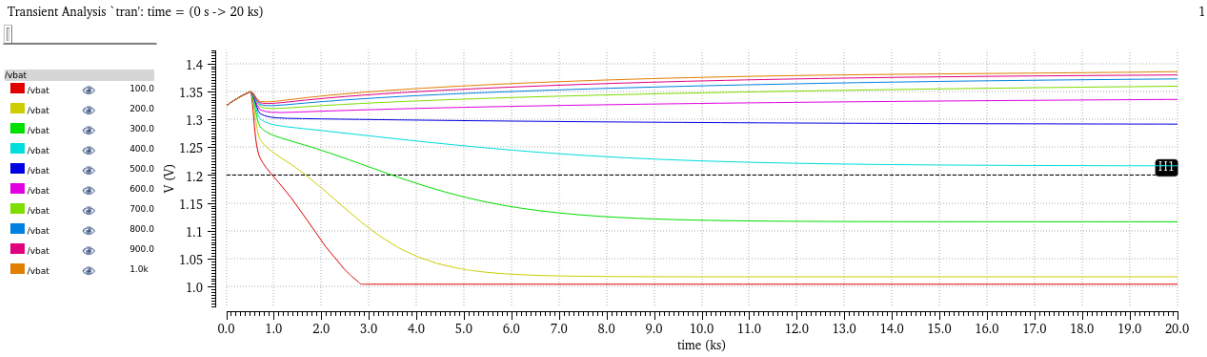

Figure 5.7: Battery's terminal voltage variation for different load values with an initial SOC of 10% and under full sun.

Table 5.3 summarizes the discharge times and current for the different load values. In this analysis, the time that it takes for the battery to discharge to 1.2 V is considered. This test can be relevant to know, for instance, for how long the battery can sustain a given voltage level, depending on the output load. Bearing in mind that the battery's initial SOC for this test is only 10%, these results lead to the conclusion that the system is able to steadily supply the load for a reasonable amount of time, while simultaneously charging the battery. For the 100 Ω load the harvested energy is not enough to continuously supply the load without discharging the battery, because the current drawn by the load is higher than the current

Table 5.3: Discharge characteristics for different load values

R_{load} (Ω)	**Discharge time to reach 1.2 V**	**Discharge current (mA)**
100	15 mn	6.2
200	26 mn	4.7
300	56 mn	3.6
400	$>$5 hours	2.9
500	-	2.6
600	-	2.1
700	-	1.9
800	-	1.7
900	-	1.5
1000	-	1.4

that the cells can supply, so after approximately 46 minutes, when the battery's voltage drops to 1 V, the discharge is interrupted. In figure 5.7, a marker highlights the points where the battery's terminal voltage reaches 1.2 V for the different load values. With 500 Ω the battery's voltage remains more or less stable, and with 600 Ω the system is able to feed the load while simultaneously charging the battery at a higher rate then the discharge rate.

5.2 System Simulation with Corners

To evaluate the system's performance under different temperatures and process variations, a corner analysis was performed. The system was tested for four different process variations related to the transistors' speed: FF (fast fast), FS (fast, slow), SF (slow, fast) and SS (slow, slow), where the first and second variation apply to the NMOS and PMOS transistors, respectively. For each of these corners, four different temperature values were selected in the range of -40ºC to 120ºC, making a total of 16 corner situations.

Figures 5.8 and 5.9 present the results obtained for the first test setup, which is the same that was used in the nominal system simulation.

The variations considered also affect the PV panel's model, altering its output voltage, which in turn affects the battery's charging rate. Figure 5.8 shows the evolution of the control signal of the second switch, as well as the battery's terminal voltage. In this scenario, it can be observed that the second switch is opened earlier for the SS corner at -40 ºC, and later for the FS corner at 125 ºC. The reason for this is due to the different input voltages, which are a consequence of the PV panel's voltage's variation with the corners, and which result in different charging rates. For SS -40 ºC the battery charges faster than for FS 125 ºC. These different charging rates are also noticeable in figure 5.9, reflected on the different I_{bat} current values for the various process variations.

The deviations observed in these results are due essentially to the changes that these process

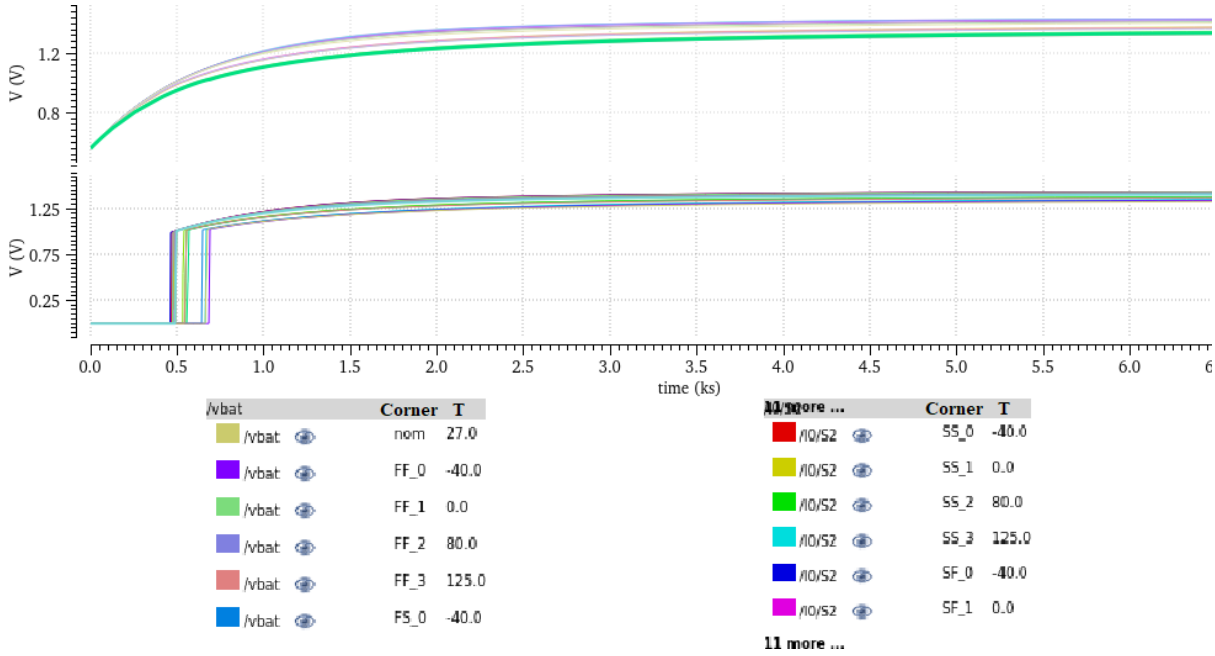

Figure 5.8: V_{bat} and switch 2 control's signal variation with corners.

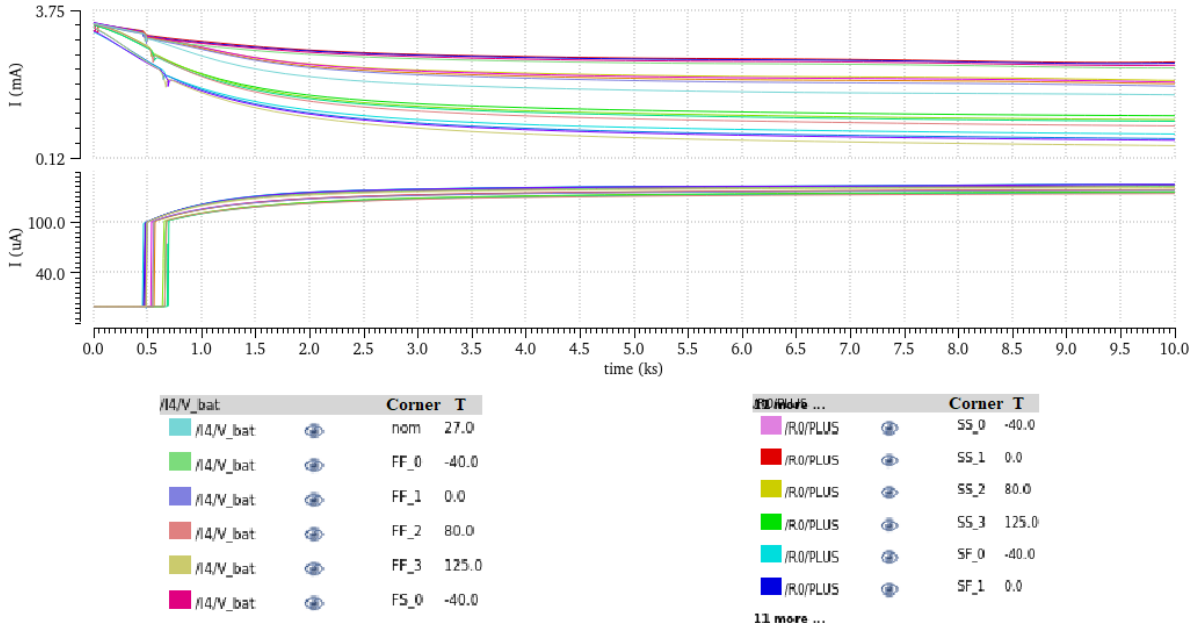

Figure 5.9: I_{bat} and I_{load} variation with corners.

variations introduce in the energy source model. Regardless of these changes, the behavior of the system is consistent with the working conditions and specified requirements, which is an indication of the validation of the system's correct operation under these different conditions.

5.3 System Validation

Taking into account all the results obtained in the previous section for the different working conditions, an evaluation of the system's validity in terms of safe operation is presented next.

To certify that the harvester is fit to operate as a battery charger for the 6VHR NiMH battery, an analysis should be made with the purpose of verifying if the developed system meets all the charging and safety recommendations supplied by the manufacturer.

According to the technical information available in [24], three charging methods are contemplated for the 6VHR battery. These methods are summarized in table 5.4.

Table 5.4: Charging methods for the 6VHR NiMH battery extracted from the datasheet

Charge method	Charging current	Charging time	Time/Voltage control
Nominal charge	0.6 mA	14-16 h	Time limited
Accelerated charge	3 mA	4h	Time limited, recommended voltage control
Trickle charge	0.18 mA (maximum)	Unlimited	Not needed

Considering the PV panel used in this work, the maximum charging current expected for the battery, is approximately 3 mA, which corresponds to the charging current indicated for accelerated charge. Despite the system not incorporating timing control, the overcharge protection implemented through voltage control certifies that the charging is interrupted when the battery reaches the EOC voltage, which typically happens before the suggested charging time is reached. Additionally, even when the PV panel is under maximum light intensity, a percentage of the available current is used to operate the remaining blocks of the system, which means that the effective current used to charge the battery is obviously lower. Taking all this aspects into consideration, it is safe to admit that a safe charging process for the battery is ensured.

6

Conclusion

Contents

6.1 Conclusions

This work allowed the completion of a solar harvester battery charger system, that meets all the initial objectives and imposed requirements. The system is capable of charging a 1.2 V battery NiMH from a nominal 1.2 V at 3.3 mA solar panel, while simultaneously supplying an end load.

Initially, a study was carried out on different equivalent circuit models that describe the electrical behavior of rechargeable NiMH batteries. An experimental procedure was developed, which consisted on applying multiple pulse-charge and pulse-discharge cycles to the battery, through the use of a Semiconductor Parameter Analyzer. Using the Analog Discovery 2 as a data logger, it was possible to measure and capture the battery's terminal voltage. Based on the battery's voltage's relaxation curve after each pulse, it was possible to estimate the model's parameters using MATLAB, for the given NiMH battery. A model was also developed for the PV panel considered in this work, using the information provided on the datasheet by the manufacturer.

Next, the harvester system was designed and fully integrated in a 65 nm CMOS process. An analysis was made on the proposed circuit solutions, based on the main specifications of the system, about the different blocks and circuits needed to accomplish it. These different blocks were then designed, and later fine-tuned, based on their behavior in the integrated system.

A full layout of the system was developed, extracted and validated. Using the models developed for the PV panel and the battery, the full system was tested in simulation, for different lightning conditions, temperatures and process variations. The reference voltages' variations were also considered and analyzed, based on an existent BGR circuit to be implemented in the same chip.

Finally, the system was validated taking into account the battery's charging/discharging requirements, and the simulation results that were obtained. The result is a 254.17 x 149.39 μm^2 fully integrated solar energy harvesting system, capable of safely charging a 1.2 V nominal NiMH battery, with overcharge and overdischarge protection.

6.2 System Limitations and Future Work

This work paves the path for many continuous improvements and possible implementations that can be done for the proposed system.

Several more complex control methods can be studied to extend the battery management techniques presented here, thus improving the system's efficiency. Introducing timing control, MPPT or a decision making circuit on when to bias the system with energy from the PV panel or from the battery are some examples of functionalities that can be explored. Another solution to be explored is the system's startup with the battery deeply discharged. This is a scenario that is presented in this work solely for simulation

purposes, but in practice should not be reached in this system since a minimum operation voltage of 1 V was considered.

Another extension of this study can also be the design of the reference voltages' generating circuit on this technology.

At last, the fabrication and testing of the system should be performed to compare with simulation results and have a more complete and detailed analysis of the system.

Bibliography

[1] N. Khosro Pour, S. Facchin, F. Krummenacher, and M. Kayal, “An ultra-low power li-ion battery charger for micro-power solar energy harvesting applications,” in *2012 19th IEEE International Conference on Electronics, Circuits, and Systems (ICECS 2012)*. Seville, Seville, Spain: IEEE, Dec. 2012, pp. 516–519. [Online]. Available: http://ieeexplore.ieee.org/document/6463695/

[2] A. A. Abdelmoaty and A. Fayed, “A single-step, single-inductor energy-harvestingbased power supply platform with a regulated battery charger for mobile applications,” in *2015 IEEE Applied Power Electronics Conference and Exposition (APEC)*. Charlotte, NC, USA: IEEE, Mar. 2015, pp. 666–669. [Online]. Available: http://ieeexplore.ieee.org/document/7104421/

[3] R. Damodaran Prabha and G. A. Rincon-Mora, “0.18-µm Light-Harvesting Battery-Assisted Charger–Supply CMOS System,” *IEEE Transactions on Power Electronics*, vol. 31, no. 4, pp. 2950–2958, Apr. 2016. [Online]. Available: http://ieeexplore.ieee.org/document/7128385/

[4] D. K. Yirenya-Tawiah, A. Blackham, A. Langford, B. Mazzeo, and S.-H. W. Chiang, “Design and Measurement of a 24.5-mW, 33-mWh, 1.8-V-Output Solar Energy Harvester for Bluetooth Sensor Nodes,” in *2022 IEEE 65th International Midwest Symposium on Circuits and Systems (MWSCAS)*. Fukuoka, Japan: IEEE, Aug. 2022, pp. 1–4. [Online]. Available: https://ieeexplore.ieee.org/document/9859409/

[5] H. Shao, C.-Y. Tsui, and W.-H. Ki, “The Design of a Micro Power Management System for Applications Using Photovoltaic Cells With the Maximum Output Power Control,” *IEEE Transactions on Very Large Scale Integration (VLSI) Systems*, vol. 17, no. 8, pp. 1138–1142, Aug. 2009. [Online]. Available: http://ieeexplore.ieee.org/document/4801595/

[6] S.-Y. Jung, M. Lee, J. Yang, and J. Kim, “A 20nW-to-140mW input power range, 94% peak efficiency energy-harvesting battery charger with frequency-sweeping input voltage monitor and optimal on-time generator,” in *2017 Symposium on VLSI Circuits*. Kyoto, Japan: IEEE, Jun. 2017, pp. C204–C205. [Online]. Available: http://ieeexplore.ieee.org/document/8008483/

[7] J. M. Amanor-Boadu, M. A. Abouzied, and E. Sanchez-Sinencio, “An Efficient and Fast Li-Ion Battery Charging System Using Energy Harvesting or Conventional Sources,” *IEEE Transactions on Industrial Electronics*, vol. 65, no. 9, pp. 7383–7394, Sep. 2018. [Online]. Available: https://ieeexplore.ieee.org/document/8258880/

[8] Tsung-Heng Tsai and Kai Chen, “A 3.4mW photovoltaic energy-harvesting charger with integrated maximum power point tracking and battery management,” in *2013 IEEE International Solid-State Circuits Conference Digest of Technical Papers*. San Francisco, CA: IEEE, Feb. 2013, pp. 72–73. [Online]. Available: http://ieeexplore.ieee.org/document/6487642/

[9] K. Kadirvel, Y. Ramadass, U. Lyles, J. Carpenter, V. Ivanov, V. McNeil, A. Chandrakasan, and B. Lum-Shue-Chan, “A 330nA energy-harvesting charger with battery management for solar and thermoelectric energy harvesting,” in *2012 IEEE International Solid-State Circuits Conference*. San Francisco, CA, USA: IEEE, Feb. 2012, pp. 106–108. [Online]. Available: http://ieeexplore.ieee.org/document/6176896/

[10] N. Khosro Pour, S. Facchin, F. Krummenacher, and M. Kayal, “An ultra-low power li-ion battery charger for micro-power solar energy harvesting applications,” in *2012 19th IEEE International Conference on Electronics, Circuits, and Systems (ICECS 2012)*. Seville, Seville, Spain: IEEE, Dec. 2012, pp. 516–519. [Online]. Available: http://ieeexplore.ieee.org/document/6463695/

[11] M. K. Rajendran, V. Priya, S. Kansal, G. Chowdhary, and A. Dutta, “A 100-mV–2.5-V Burst Mode Constant on-Time-Controlled Battery Charger with 92% Peak Efficiency and Integrated FOCV Technique,” in *2020 IEEE International Symposium on Circuits and Systems (ISCAS)*. Seville, Spain: IEEE, Oct. 2020, pp. 1–1. [Online]. Available: https://ieeexplore.ieee.org/document/9180424/

[12] A. A. Blanco and G. A. Rincon-Mora, “Compact Fast-Waking Light/Heat-Harvesting 0.18-μm CMOS Switched-Inductor Charger,” *IEEE Transactions on Circuits and Systems I: Regular Papers*, vol. 65, no. 6, pp. 2024–2034, Jun. 2018. [Online]. Available: https://ieeexplore.ieee.org/document/8100622/

[13] R. R. Thakkar, Y. Rao, and R. R.Sawant, “Performance Analysis of Electrical Equivalent Circuit Models of Lithium-ion Battery,” in *2020 IEEE Pune Section International Conference (PuneCon)*. Pune, India: IEEE, Dec. 2020, pp. 103–107. [Online]. Available: https://ieeexplore.ieee.org/document/9362386/

[14] M. Chen and G. Rincon-Mora, “Accurate Electrical Battery Model Capable of Predicting Runtime and I–V Performance,” *IEEE Transactions on Energy Conversion*, vol. 21, no. 2, pp. 504–511, Jun. 2006. [Online]. Available: http://ieeexplore.ieee.org/document/1634598/

[15] A. Hentunen, T. Lehmuspelto, and J. Suomela, “Time-Domain Parameter Extraction Method for Thévenin-Equivalent Circuit Battery Models,” *IEEE Transactions on Energy Conversion*, vol. 29, no. 3, pp. 558–566, Sep. 2014. [Online]. Available: http://ieeexplore.ieee.org/document/6811175/

[16] H. Rahimi-Eichi and M.-Y. Chow, “Adaptive parameter identification and State-of-Charge estimation of lithium-ion batteries,” in *IECON 2012 - 38th Annual Conference on IEEE Industrial Electronics Society*. Montreal, QC, Canada: IEEE, Oct. 2012, pp. 4012–4017. [Online]. Available: http://ieeexplore.ieee.org/document/6389248/

[17] S. Abu-Sharkh and D. Doerffel, “Rapid test and non-linear model characterisation of solid-state lithium-ion batteries,” *Journal of Power Sources*, vol. 130, no. 1-2, pp. 266–274, May 2004. [Online]. Available: https://linkinghub.elsevier.com/retrieve/pii/S0378775303011455

[18] A. Technologies and EasyEXPERT, “Agilent 4156c precision semiconductor parameter analyzer,” 2001. [Online]. Available: https://www.keysight.com/us/en/product/4156C/precision-semiconductor-parameter-analyzer.html#

[19] I. Digilent, “Analog discovery 2 and waveforms.” [Online]. Available: https://digilent.com/shop/analog-discovery-2-100ms-s-usb-oscilloscope-logic-analyzer-and-variable-power-supply/

[20] W. Li, L. Liang, W. Liu, and X. Wu, “State of Charge Estimation of Lithium-Ion Batteries Using a Discrete-Time Nonlinear Observer,” *IEEE Transactions on Industrial Electronics*, vol. 64, no. 11, pp. 8557–8565, Nov. 2017. [Online]. Available: http://ieeexplore.ieee.org/document/7926321/

[21] J. Cubas, S. Pindado, and C. de Manuel, “Explicit Expressions for Solar Panel Equivalent Circuit Parameters Based on Analytical Formulation and the Lambert W-Function,” *Energies*, vol. 7, no. 7, pp. 4098–4115, Jun. 2014. [Online]. Available: http://www.mdpi.com/1996-1073/7/7/4098

[22] N. Khosropour, F. Krummenacher, and M. Kayal, “Fully integrated ultra-low power management system for micro-power solar energy harvesting applications,” *Electronics Letters*, vol. 48, no. 6, p. 338, 2012. [Online]. Available: https://digital-library.theiet.org/content/journals/10.1049/el.2012.0315

[23] G. Traversi, F. D. Canio, L. Gaioni, M. Manghisoni, L. Ratti, and V. Re, “Design of bandgap reference circuits in a 65 nm CMOS technology for HL-LHC applications,” *Journal of Instrumentation*, vol. 10, no. 02, pp. C02 004–C02 004, Feb. 2015. [Online]. Available: https://iopscience.iop.org/article/10.1088/1748-0221/10/02/C02004

[24] V. Microbattery, “Rechargeable button cells nimh - sales program and technical handbook.” [Online]. Available: https://www.varta-ag.com/fileadmin/varta_microbattery/downloads/

service/battery-documentation/nickel-metal-hydride/Sales-Literature-201810_HANDBOOK_Rechargeable_Button_Cells_NiMH_en.pdf

A

Battery characterization experimental procedure

A.1 Apendix A: Battery characterization experimental procedure

The Parameter Analyzer 4156C can be used to perform current-controlled charge and discharge tests on the battery, while providing a means to accurately measure its terminal voltage simultaneously. In order to do so the following procedure should be carried out.

A.1.1 Setting up the devices

1. Start off by installing the *EasyExpert* software in your computer. This software will be used to create the application programs to test the device under test.

2. Attach the parameter analyzer to the test fixture, performing the connections presented in figure A.1.

[4146C.] 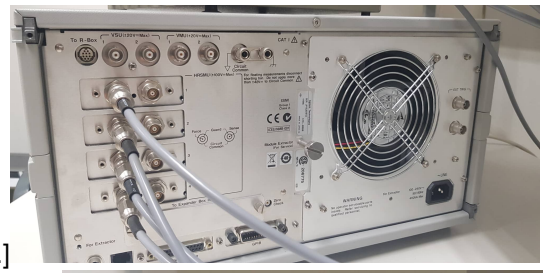 [Test fixture.] 

Figure A.1: Device connections.

3. Connect the Parameter Analyzer to your computer through the GPIB cable.

4. Placing the battery in the test fixture, connect the positive terminal to SMU1 and the negative terminal to ground, according to figure A.2.

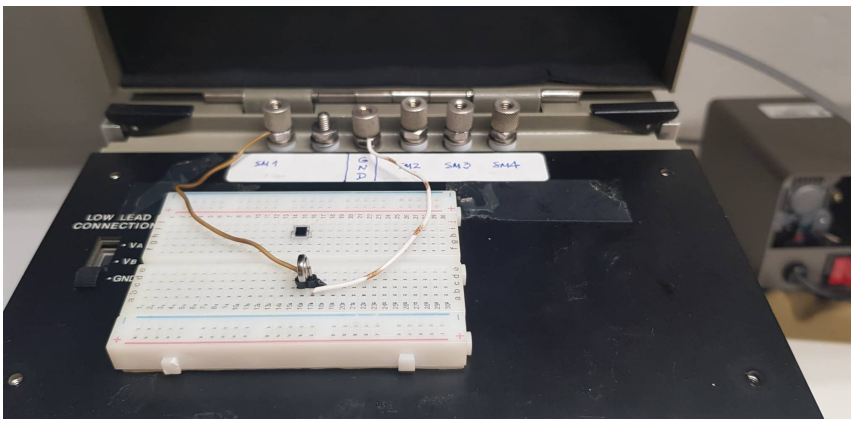

Figure A.2: Battery connection to test fixture.

A.1.2 Setting up the test system

After setting up all the equipment, an application test should be created for the DUT. In this case two applications are exemplified, one to continuously charge/discharge the battery with constant current, and another one to pulse charge/discharge the battery for a specified period of time.

A.1.2.A Constant charge/discharge application

For the constant charge/discharge, the pre-defined I/V-t sampling classic test can be used, with some small adjustments.

1. On *EasyExpert* select *Classic Test* on the left panel and choose **I/V-t Sampling**.

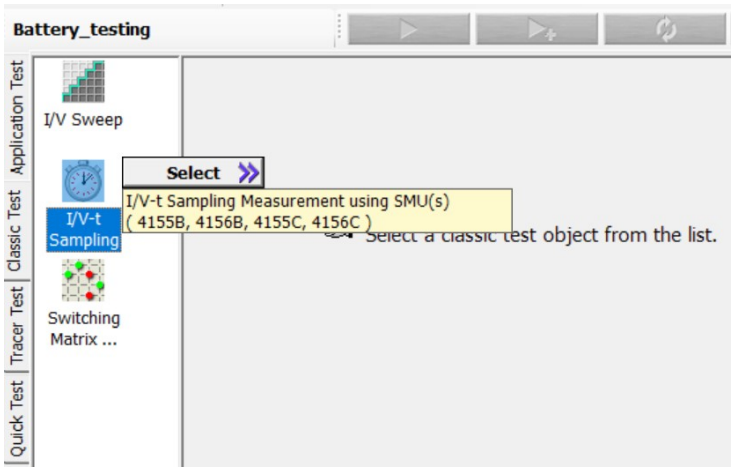

Figure A.3: Selecting *I/V-t Sampling* test.

2. Specify the test parameters. In the channel definition choose the source from which the current should be applied (**Unit**), enter the voltage and current names and specify the **Mode** as voltage or current to define the constant variable. In this case, constant current is selected.

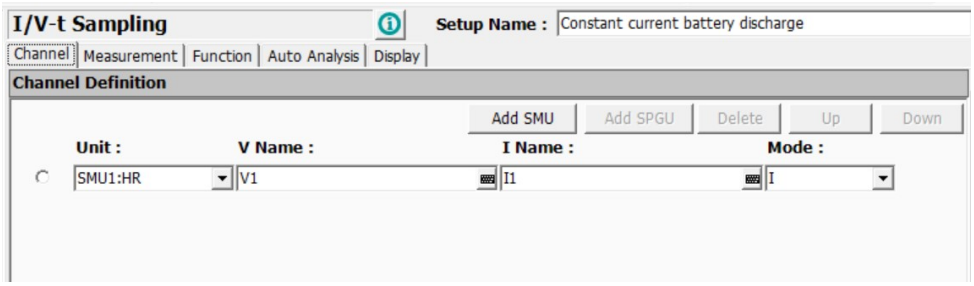

Figure A.4: Test parameters.

3. On the *Measurement* tab enter the **Sampling Interval** and **Number of Samples** according to the test duration intended and enter a **Hold Time** if an initial delay is needed. In the bottom window specify the constant current value **Source** and the **Compliance Voltage**. This voltage represents the maximum voltage a current source can reach while attempting to produce the desired current. I should be guaranteed that this value is greater than the expected terminal voltage of the battery.

4. The *Display* can be used to specify the output signals to be saved and viewed during the test.

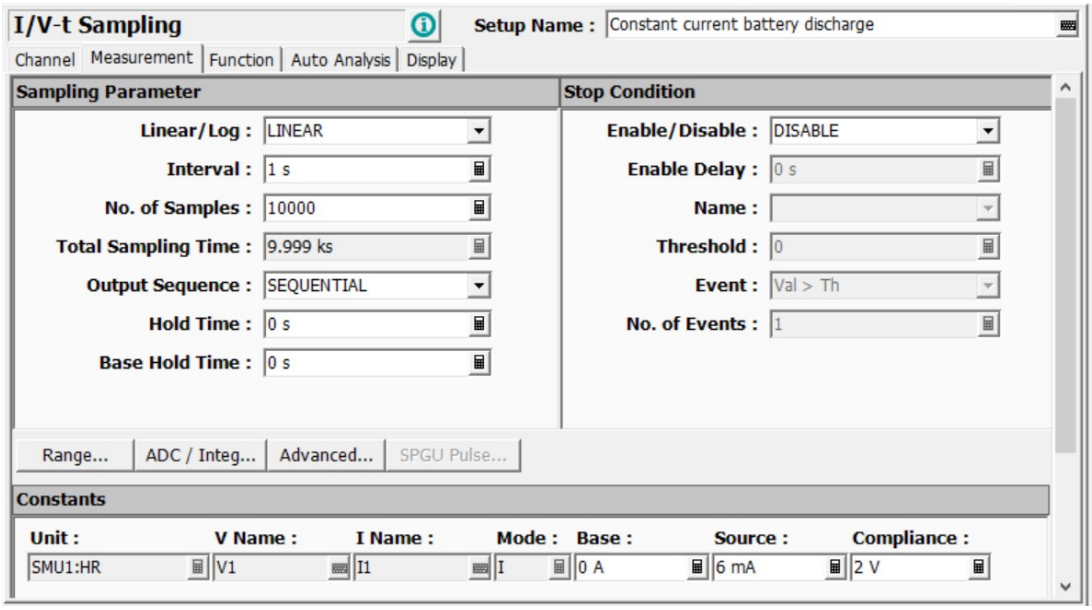

Figure A.5: Measurement configurations.

5. Initiate the test by pressing the green button on top. When the test begins, an additional window is opened where the current and terminal voltage of the battery can be seen in real time.

6. After the test completion, the experimental data can be saved from the waveform window both as an image file and as excel data.

A.1.2.B Pulse charge/discharge application

For the pulse charge/discharge, a custom application test needs to be created.

1. Right-clicking the *Library* sub-window and select **New**. An additional window is opened where the new application will be defined.

2. In the new window input the test name and the test parameters definition, as shown in figure A.8.

3. Switching to the **Contents** tab, the test program list can be defined as presented in figure A.9.

   In this test a current pulse is built based on the I/V-t Sampling classic test, by continuously applying a constant current value, followed by a relaxation period of zero current. In the example, this cycle is repeated 20 times. To create the *PulseDischarge* and *Relaxation* programs select **I/V-t Sampling** from the *Classic Tests* on the left panel and fill the test parameters following the same procedure described above. For the *PulseDischarge* the total sampling time selected was 360 s with the *Isource* value as the constant current and for the *Relaxation* program 600 s was selected with zero current.

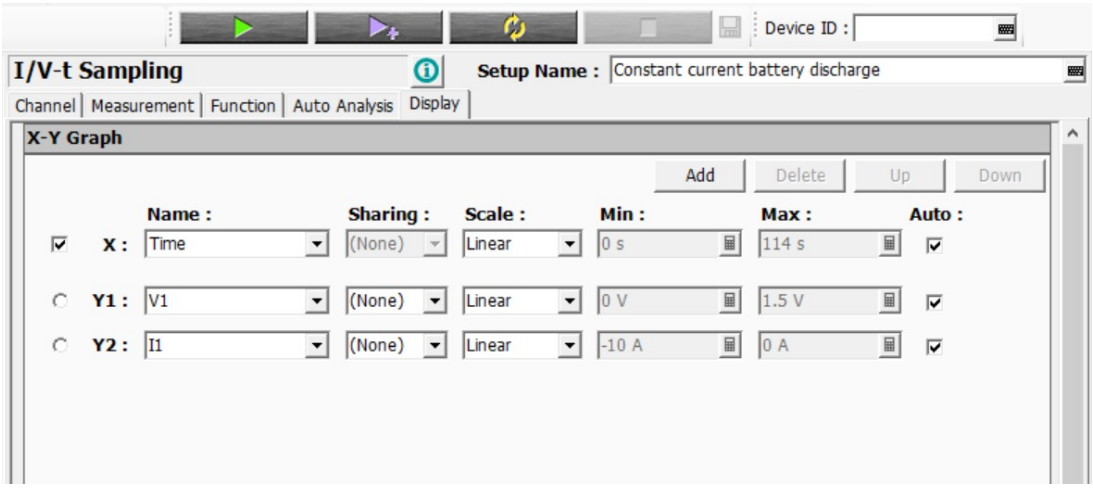

Figure A.6: Display options.

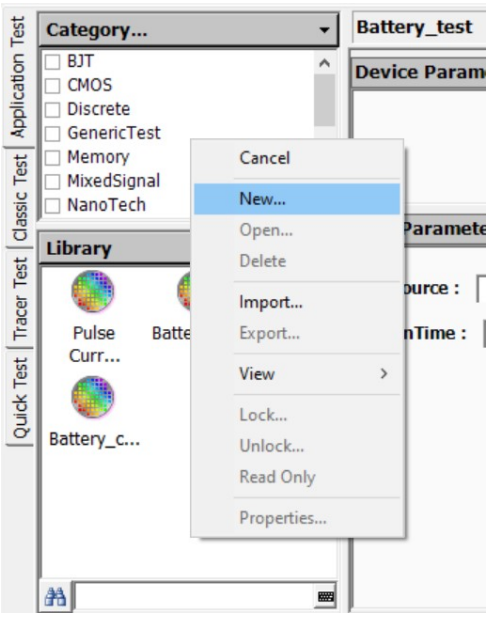

Figure A.7: Creating a new application test..

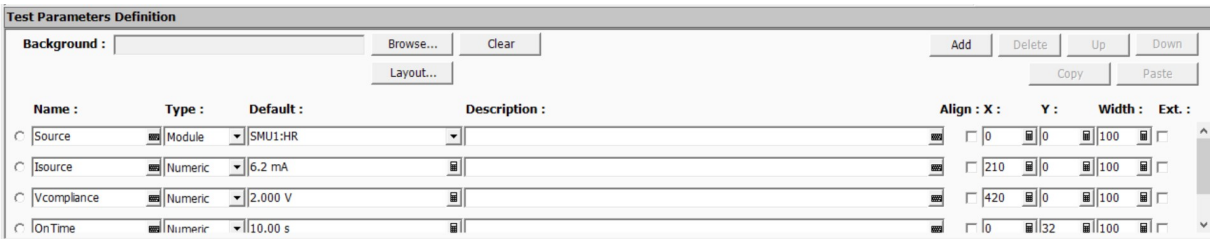

Figure A.8: Test specifications.

4. Save the custom test by clicking *File* $\longrightarrow$ *Save*. Once the test is saved it can always be edited by right-clicking it and selecting the *Open* option.

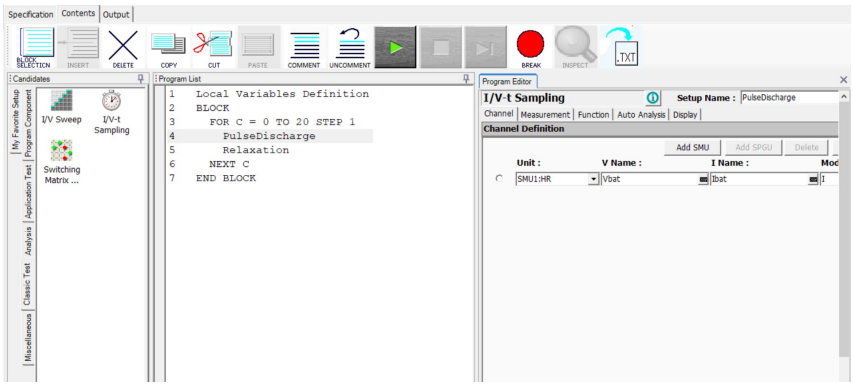

Figure A.9: Test contents.